PREDICTING HYDRAULIC FRACTURE CONDUCTIVITY IN SHALE PLAYS

A Thesis

by

CODY JAMES KAINER

Submitted to the Office of Graduate and Professional Studies of
Texas A&M University
in partial fulfillment of the requirements for the degree of

MASTER OF SCIENCE

Chair of Committee,	Ding Zhu
Co-Chair of Committee,	A. Daniel Hill
Committee Member,	Benchun Duan
Head of Department,	A. Daniel Hill

August 2017

Major Subject: Petroleum Engineering

ABSTRACT

The purpose of hydraulic fracturing in low permeability shales is to maximize surface contact area with the reservoir and create conductive flow paths for the hydrocarbons to be economically produced through. Fracture conductivity is defined as the product of fracture permeability (k_f) and the width of the fracture aperture (w_f). This parameter is vital, as it limits the capacity of the flow path between the stimulated reservoir rock and the wellbore for a given drawdown pressure. The resulting fracture conductivity is dependent on a plethora of rock and proppant properties. Realistic prediction of conductivity and further understanding of its relationship with rock properties would prove incredibly valuable, especially in new and developing shale plays where there is a steep initial learning curve in economic production. In this study, multiple linear regression is applied to a large database of shale conductivity experiments, and a robust correlation for predicting conductivity is presented. In addition, the properties of Young's modulus, Poisson's ratio, compressive strength, and Brinell hardness are isolated and their effects on fracture conductivity are analyzed.

The shale plays included in the correlations are the Barnett, Fayetteville, Marcellus, and Eagle Ford shales. Brinell hardness and compressive strength were found to be highly correlated with conductivity decline as closure stress increases. Young's modulus was also found to be a highly significant predictor of fracture conductivity in shales. A higher modulus correlated to increased conductivity at each closure stress. It was also concluded that closure stress and proppant loading conditions have a much

greater influence on fracture conductivity when compared to rock mechanical properties and fracture surface characteristics. The final correlation model presented can be used to estimate fracture conductivity in various shale plays. It is important to keep in mind the distributions of the input data into the model, as well as the experimental conditions under which the conductivity was measured when applying this correlation for prediction purposes.

DEDICATION

I would like to dedicate this work to my family, who pushed me to achieve a higher level of education and supported me unconditionally at every step of the way.

ACKNOWLEDGEMENTS

I would like to thank my advisor, Dr. Zhu, for allowing me to join her fracture conductivity group and providing her wisdom over the years. I would also like to acknowledge Dr. Hill and Dr. Duan for their guidance and support throughout the course of this research.

Thanks to other members of the research group over the past few years, namely, Dante Guerra, Omar Enriquez-Tenorio, Ashley Knorr, and Bill Foran for the knowledgeable discussions and the passing on of your expertise. Special thanks to Jesse Guerra, Kevin Wylie and Ryan Winner for help with performing the conductivity experiments. I wish you all the best of luck in your studies and future endeavors in the real world.

I would like to acknowledge the Department of Energy and the Research Partnership to Secure Energy for America (RPSEA) for their financial support of this work.

Finally, thanks to all of the friends I have made along the way and the distractions you all provided. Especially Stephanie Sylvester, who has always been there for me throughout this process.

CONTRIBUTORS AND FUNDING SOURCES

This work was supervised by a thesis committee consisting of advisor Dr. Ding Zhu and Dr. A. Daniel Hill of the Department of Petroleum Engineering and Dr. Benchun Duan of the Department of Geology and Geophysics.

The data analyzed for the fracture conductivity correlation relative to each shale formation was provided by Anton Kamenov (Barnett), Junjing Zhang (Barnett), Kathryn Briggs (Fayetteville), Timothy Jansen (Fayetteville), Mark McGinley (Marcellus), Paola Perez-Pena (Marcellus), Omar Enriquez-Tenorio (Eagle Ford), and Ashley Knorr (Eagle Ford).

All other work conducted for the thesis was completed by the student independently under the advisement of his committee.

This work was made possible in part by the Department of Energy and the Research Partnership to Secure Energy for America (RPSEA) under Project Number 11122-07.

TABLE OF CONTENTS

Page

Page

LIST OF FIGURES

Page

Page

Page

LIST OF TABLES

Page

1. INTRODUCTION

1.1 Background

During the hydraulic fracturing process in low permeability shales, various types of proppant and fluid are pumped into the reservoir with the goal of generating an optimal fracture network with an optimal fracture conductivity distribution. Fracture conductivity is defined as the product of permeability inside the fracture (k_f) and the width of the fracture aperture (w_f). This parameter is vital as it limits the capacity of the flow path between the stimulated reservoir rock and the wellbore, for a given drawdown pressure. Each shale formation is unique with large variations in matrix/unpropped deliverability, mechanical properties, mineralogy, fluid sensitivities and closure stress, all of which affect the optimal stimulation treatment and resulting fracture conductivity. Realistic prediction of conductivity and further understanding of its relationship with rock properties would prove incredibly valuable, especially in new and developing shale plays where there is a steep initial learning curve in economic production.

1.2 Literature Review

The literature review is divided into three sections. The first section discusses current methodologies of measuring fracture conductivity in the lab and key experimental conditions in each setup. The second section discusses a majority of the mechanisms affecting conductivity inside the reservoir. Lastly, previous research conducted at Texas A&M University concerning shale fracture conductivity is discussed.

1.2.1 Laboratory Measurement of Conductivity

Fracture conductivity measurements in the laboratory began with Cooke (1973), where the permeability of a ½ in. thick pack of varying proppant sizes was tested under increasing closure stresses with oil, brine, and gas fluids at reservoir temperatures. Cooke's work served as a precursor to the development of the standard API RP 61 (1989) procedure for measuring conductivity. Important conditions from the procedure include:

-2 lbm/ft^2 proppant loading

-Steel pistons in contact with the proppant to apply load

-Room temperature

-2% KCL flowed at 2 ml/min

The goal of this standard was to reliably test the performance of different types of proppant, but it neglected many factors found at reservoir conditions. More recently, the International Organization for Standardization released ISO 13503-5 (2006), which uses sandstone cores in contact with the proppant and maintains each stress for 50 hours at 150-250°F. Researchers have modified these procedures and used other methods to study the effects of different conditions on fracture conductivity. These conditions are highlighted in the next section.

1.2.2 Mechanisms Affecting Conductivity

According to the definition of fracture conductivity, a decrease in fracture width or permeability causes a decrease in conductivity. Initial width is controlled by areal concentration and size of the proppant. Effective closure stress on the fracture dominates

width reduction by exacerbating proppant crushing/rearrangement and proppant embedment into the fracture face (Terracina et al. 2010, Huitt and McGlothlin 1958). Alramahi and Sundberg (2012) investigated proppant embedment in shales, in the absence of fluids, and related it to the rocks mineral composition and mechanical properties. They concluded that samples with high clay content and/or low static Young's modulus resulted in higher embedment. The authors were also able to derive a power law expression relating proppant embedment to Young's modulus, more evident at closure stresses greater than 3,000 psi. Cooke (1975) began studying the effects of fluids on conductivity, specifically viscous guar based treatment fluid and the reduction in permeability caused by the residue it leaves behind. Others studied fluid effects on conductivity loss in shales primarily due to increased proppant embedment from water-rock interactions on the fracture face (Akrad et al. 2011; Das and Achalpurkar, 2013; Zhang et al. 2014; Guerra et al. 2017). The consensus is that higher clay content leads to an increase in clay swelling and surface softening, causing proppant to embed further into the rock. Ramurthy et al. (2011) suggested using the Brinell hardness test on wet and dry shale samples to quantify the degree of expected proppant embedment. The Brinell hardness measurement is discussed further in the experimental methods section. Mueller and Amro (2015) took the principle of surface hardness further and developed a numerical model in order to predict proppant embedment. Primary inputs into the model were proppant size distribution, surface hardness, and stress on the proppant.

Another important area of consideration is fracture surface effects, particularly in areas of low proppant concentration where surface interactions are likely. Barton et al.

(1985) examined the mechanical behavior of rock joints and coupled this with conductivity. Using data from tilt tests and Schmidt rebound tests, the authors concluded that weak rocks with smooth joints close the easiest, while rougher surfaces with high strength are harder to close under normal stress. Makurat and Gutierrez (1996) expanded on this work and found that shear displacement of the fracture faces can significantly increase conductivity in weak rocks and is dependent on a surface roughness coefficient. Fredd et al. (2001) investigated very low proppant concentrations often found in slickwater fracs where mono to partial monolayers of proppant exist. The authors concluded that conductivity can be either asperity dominated or proppant dominated, depending on the concentration, and *"under asperity dominated conditions, the conductivity varies significantly and is difficult to predict."*. Parker et al. (2005) showed that these high porosity, partial monolayer propped fractures can result in even higher conductivity than those with larger proppant concentrations.

Conditions not accounted for in the standard procedures mentioned earlier for measuring conductivity include non-Darcy flow effects, multiphase flow, cyclic stress on the proppant, and fines migration, among other effects. It is common to see reductions in conductivity of 95% compared to ISO 13503-5 when all of these conditions are taken into account (Palisch et al. 2007). Barree et al. (2003) also looked at the combined effects and concluded that actual reservoir conductivity based on laboratory results is much lower than believed or expected.

1.2.3 Previous Research at Texas A&M University

Over previous years, researchers from the petroleum engineering department at Texas A&M University have amassed a large database consisting of conductivity measurements and rock properties from major shale plays across the United States. These are, in chronological order, the Barnett (Kamenov 2013; Zhang 2014), Fayetteville (Briggs 2014; Jansen 2014), Marcellus (McGinley 2015; Perez Pena 2015), and Eagle Ford (Enriquez-Tenorio 2016; Knorr 2016). The conductivity experiments were short-term tests, with nitrogen flowing through induced fractured samples at proppant concentrations usually less than .3 lb/ft^2. In addition, Zhang (2014) and Guerra (2017) studied the effects of water damage on the Barnett and Eagle Ford shales respectively, in which gas conductivities were compared before and after water flow through the fracture. It is in consensus from these studies that conductivity behavior is controlled by a combination of proppant, rock, and fracture surface properties. A higher Young's modulus has in general correlated to higher values of both propped and unpropped conductivity. More recently in the Eagle Ford dataset, an inverse relationship was found between Poisson's ratio and conductivity, while rock brittleness calculated from mineralogy showed a direct relationship (Enriquez-Tenorio et al. 2016). Fracture surface roughness has also shown to be a predictive parameter, especially in proppant monolayer conditions. Brinell hardness has only been investigated in the Eagle Ford and no definitive conclusions regarding this parameter could be made. Mineralogy was shown to be highly significant in predicting conductivity loss due to rock-water interactions.

1.3 Problem Description

A correlation for estimating shale fracture conductivity based on experimental data is lacking in the literature. The only experimental correlation for predicting propped fracture conductivity was recently published by Barree et al. (2016) and is based on over 1,000 conductivity experiments. Tests were ran with 2% KCL brine under Darcy flow conditions. Each stress and flow condition was maintained for 50 hours at a standard test temperature of 150°F. Relatively high proppant concentrations above 1 lb/ft^2 were used. Smooth faced slabs of fine-grained Ohio sandstone, with a Young's modulus of 5 X 10^6 psi, applied stress to the proppant pack in all experiments. This correlation may not be suitable for the more realistic proppant concentrations of less than 1 lb/ft^2 or any varying rock properties, which have been shown to have significant effects on fracture conductivity under reduced proppant loadings, as discussed earlier.

Although significant conclusions could be made regarding the relationship of static Young's modulus and Poisson's ratio to fracture conductivity, their sole effects were unclear due to the multitude of other variables present. This study also isolates the mechanical properties of Young's modulus, Poisson's ratio, compressive strength, and Brinell hardness. This allows concrete description/quantification of their effects on conductivity inside the fracture as well as in the experimental setup, where only vertical stress is controlled and measured.

1.4 Research Objectives and Significance

The primary objectives of this work are as follows:

(1) Develop a robust correlation which industry can use to more realistically estimate fracture conductivity in the new and existing shale plays, based on varying proppant types, proppant concentrations, and rock properties.

(2) Gain further understanding of the effects that mechanical rock properties have on fracture conductivity. Namely Young's modulus, Poisson's ratio, compressive strength, and Brinell hardness. Accomplish this by eliminating variables in previous experiments used for the correlation and selecting rock samples with a large range of mechanical properties.

(3) Perform conductivity, triaxial, and Brinell hardness tests on the selected rock samples.

(4) Provide recommendations for future work in this area for more robust characterization of each rock sample, enabling more accurate prediction of fracture conductivity at reservoir conditions.

The results of this study prove valuable, as there is usually a steep learning curve in achieving economic production due to uncertainties in fracture conductivity (Palisch et al. 2007).

1.5 Structure of Thesis

Following the introduction and experimental methodologies there are two main parts to this thesis. The first is concerned with the analysis of historical data gathered by previous researchers at Texas A&M University and the generation of a shale conductivity correlation. The second part is a set of conductivity and rock property experiments

designed to complement the correlations by examining the relationship/s between Young's modulus, Poisson's ratio, compressive strength, Brinell hardness, and fracture conductivity.

2. EXPERIMENTAL DESIGN AND METHODOLOGY

This section discusses experimental setups and laboratory procedures used to measure properties in the conductivity correlation as well as variables investigated in the mechanical effects study. The multiple linear regression technique used to generate the correlations is also presented.

2.1 Experimental Design

All experiments used for the shale conductivity correlations were conducted by previous researchers. Experimental design for each shale formation is discussed in the results section. However, new experiments were performed to fill gaps in the previous work and provide insight into better characterization of rock properties relating to fracture conductivity. Initial sample selection for the rock property study was explicitly based on achieving a broad range of mechanical properties for conductivity testing. The four rock types selected were Austin chalk, Lueders limestone, Crab Orchard sandstone, and Castlegate sandstone. The performed experimental design matrix is shown below in **Table 1**.

Table 1-Performed experiments on the selected rock types.

Formation	Fracture Conductivity		Triaxial		Brinell Hardness	
	# of Samples	# of Successful Tests	# of Samples	# of Sucessful Tests	# of Samples	# of Successful Tests
Austin Chalk	3	2	3	2	1	6
Lueders Limestone	3	2	2	2	1	6
Crab Orchard Sandstone	3	2	3	3	1	6
Castlegate Sandstone	3	3	2	2	1	6

The proppant of choice for conductivity testing was 30/50 mesh, high-density ceramic with a low API crush value of 2.6% at 5,500 psi. This value means that 2.6% by weight of a 4 lb/ft^2 proppant pack was crushed into smaller particles while undergoing 5,500 psi of vertical stress in a confined environment. A strong proppant mitigates the fracture width reduction caused by proppant crushing/deformation and exacerbates the effects of proppant embedment on conductivity, which are controlled by closure stress and properties of the rock itself. An areal proppant concentration of .3 lb/ft^2 on the fracture face was used, resulting in a minimum of two proppant layers spread evenly across the fracture face. This concentration avoided proppant monolayer conditions but still allowed rock properties to have a significant role in the resulting conductivity. Milled fracture surfaces were used to keep roughness and surface asperity effects consistent between samples. **Figure 1** shows a sample face loaded with .3 lb/ft^2 of 30/50 mesh ceramic proppant, demonstrating full coverage of the fracture surface and approximately two layers of proppant.

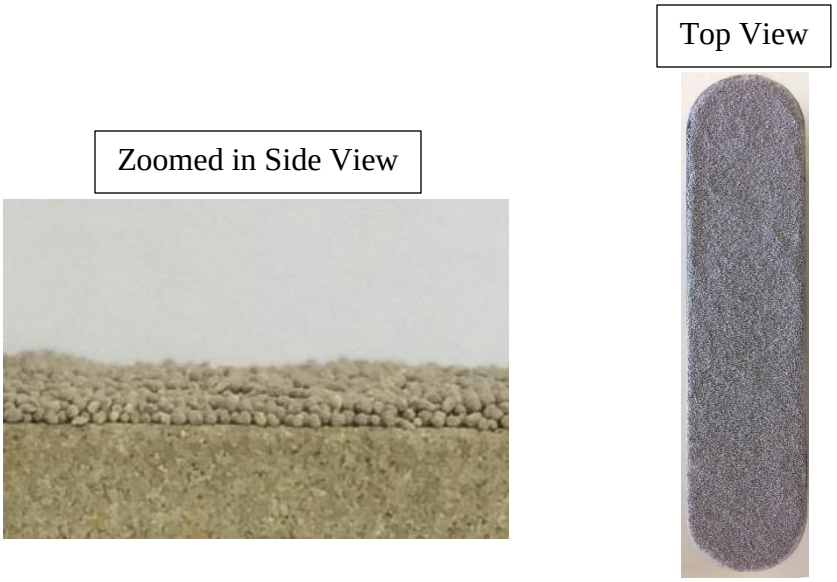

Figure 1-Sample loaded with .3 lb/ft^2 proppant concentration.

2.2 Fracture Conductivity

The fracture conductivity setup and procedure discussed here was used in the rock properties study as well as by the previous researchers during compilation of the shale conductivity database. The key difference between the two arises in the sample preparation, with milled vs. induced fracture surfaces respectively. Conductivity was measured using a modified API RP-61 procedure and experimental setup as detailed by many previous researchers (Kamenov 2013; Briggs 2014; Guzek 2014; Zhang 2014; McGinley 2015; Enriquez-Tenorio 2016). Because the setup and procedure are so well documented, only an overall summary and key characteristics are mentioned. The samples have dimensions of 1.5" wide, 7" long, and an ideal thickness of 6". Variations in thickness result from the fragility of the shale samples during cutting, in which case sandstone inserts are used to make up the entire 6". The samples are placed in a confined

conductivity cell with a hydraulic load frame providing vertical stress to the pistons. Tests begin at a low closure stress of 500 to 1,000 psi and are ramped up in 500 to 1,000 psi increments until a maximum desired stress level is reached, or the sample fails. Nitrogen is used as the test fluid to simulate natural gas flowing through the fracture. Nitrogen also does not damage the precious samples and allows them to be reused in consecutive tests. The experimental setup is detailed in **Figure 2**.

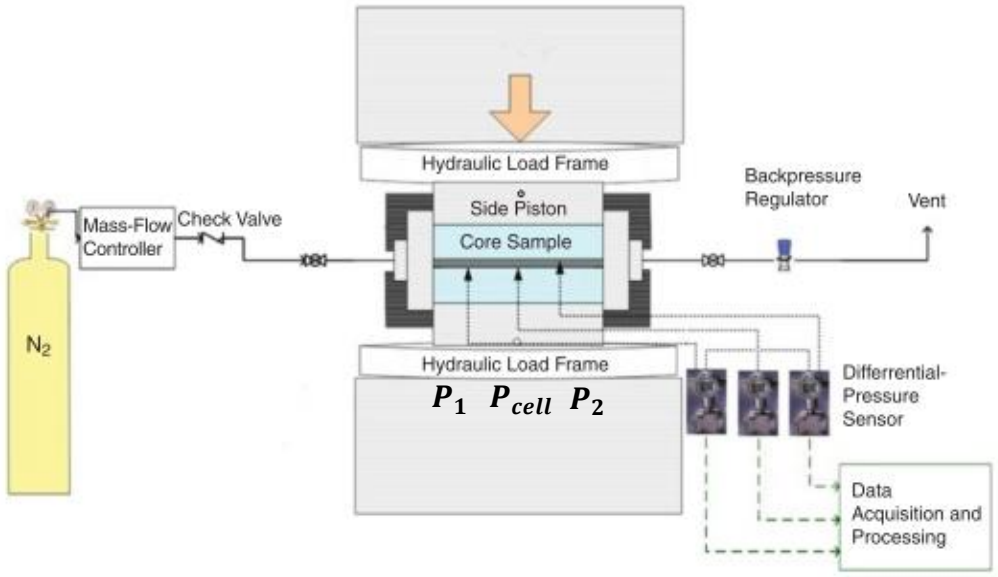

Figure 2-Fracture conductivity experimental setup (modified from Zhang 2014).

Pressure drop across the sample is measured using a differential pressure transducer and the Darcy's law concept, represented by **Eq. 1,** is applied to calculate the conductivity. At each closure stress level, four pressure drops and their corresponding flow rates are recorded under steady state conditions to reduce measurement error.

$$-\frac{dp}{dL} = \frac{\mu v}{k_f} \quad \text{(1)}$$

In instances where non-Darcy/turbulent flow conditions exist due to higher flow rates required to achieve a pressure drop, Forchheimer's equation is used. This equation, shown in **Eq. 2**, adds a pressure drop term due to inertial effects caused by turbulence.

$$-\frac{dp}{dL} = \frac{\mu v}{k_f} + \beta \rho_f v^2 \quad \text{(2)}$$

As applied to this experimental setup, $-\frac{dp}{dL}$ is the pressure drop across the fracture per unit length between the differential pressure ports, μ is the viscosity of nitrogen, v is the flow velocity, k_f is the permeability inside the fracture, ρ_f is the density of nitrogen, and β is the inertia resistance factor. Actual values recorded in this setup are nitrogen volumetric flow rate (Q), the pressure at the center of the fracture (P_{cell}), and the pressure drop between the two outer pressure ports (ΔP). Integrating Eqs. 1 and 2 and applying the ideal gas law along with conservation of mass, Tek et al. (1962) derived the general forms of the Darcy and Forchheimer equations. By assuming **Eq. 3** and **Eq. 4** hold true, Eq. 1 and Eq. 2, from their general forms, can be expressed as **Eq. 5** and **Eq. 6**,

$$P_1 = P_{cell} + .5\Delta P \quad \text{(3)}$$

$$P_2 = P_{cell} - .5\Delta P \quad \text{(4)}$$

$$\frac{2P_{cell}\Delta PM_g}{2ZRTL} = \frac{\mu\rho Q}{h_f}\frac{1}{C_f} \quad \text{.....(5)}$$

$$\frac{2P_{cell}\Delta PM_g h_f}{2ZRTL\mu\rho Q} = \frac{\rho Q}{\mu h_f}\frac{\beta}{w_f^2} + \frac{1}{C_f} \quad \text{.....(6)}$$

where C_f is fracture conductivity, M_g is the molar mass of nitrogen, h_f is the sample width, Z is the gas compressibility factor, R is the universal gas constant, T is temperature, and w_f is the fracture width. Therefore, in Darcy flow (Eq. 5), the inverse of the slope of the line representing $\frac{2P_{cell}\Delta PM_g}{2ZRTL}$ vs. $\frac{\mu\rho Q}{h_f}$ is equal to fracture conductivity. For turbulent flow (Eq. 6), the inverse of the y-intercept while plotting $\frac{2P_{cell}\Delta PM_g h_f}{2ZRTL\mu\rho Q}$ vs. $\frac{\rho Q}{\mu h_f}$ is equal to the conductivity of the fracture. These are the two governing methods used to calculate fracture conductivity, with outputs from the experimental setup and nitrogen fluid characteristics. The volumetric flow rates when each equation is applicable is highly dependent upon proppant concentration, which controls the fracture area open to flow and in turn, the gas velocity. McGinley (2015) found that Darcy's law provided a good fit for concentrations below .1 lb/ft^2 with flow rates below 2 L/min. For the rock properties study, all flow rates were kept within the Darcy flow regime.

2.3 Mechanical Properties

The static Young's modulus and Poisson's ratio along with compressive strength were measured by means of a triaxial compression test. This test was conducted according to the American Society for Testing and Materials (ASTM) standard test methods for compressive strength and moduli of intact rock core specimens under varying states of stress and temperature, known as ASTM D7012-14. Sample specimens were cut in the shape of cylinders with a diameter of one inch and a length of two inches. All samples are tested using a confining stress of 2 MPa (≈290 psi) to ensure sample stability. Multiple loading and unloading cycles were applied to rid the sample of any initial inelastic deformation. The axial compressive stress was increased until sample failure in most instances. The procedure and experimental setup has been thoroughly discussed by Jansen (2014), Perez-Pena (2015), and Knorr (2016). Two linear variable differential transformers (LVDT) are used to measure axial deformation of the sample. A chain gauge containing another LVDT measures a change in chord length, which is then converted to the circumferential deformation of the sample. The LVDTs are sensitive to .0001 millimeters of displacement. **Figure 3** shows a fully prepared sample ready to be placed into the triaxial cell.

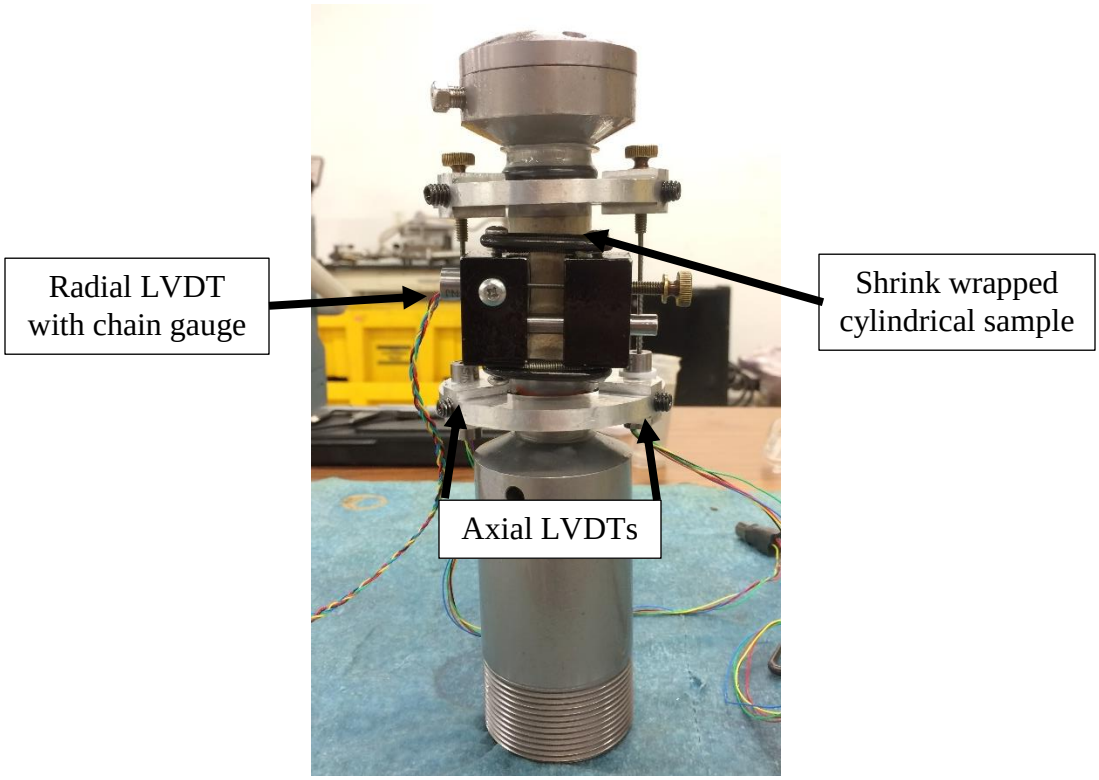

Figure 3-Fully prepared Austin Chalk sample with LVDTs and chain gauge to measure axial and radial strains.

The sample is then placed inside the triaxial cell, where confining pressure is applied by hydraulic oil and a hydraulic piston provides the axial load. **Figure 4** shows the sample inside the cell, ready for the first loading cycle to be applied.

Figure 4-Sample inside the triaxial cell awaiting the first load cycle.

It is vital to ensure the LVDTs are communicating with the GCTS software, have enough range to capture the expected deformation, and remain located within their optimal operating range of +/- 1.5 mm during the test. Axial and radial strain values are then plotted from the results, with axial stress on the y-axis. Average slope of the straight-line portion from each stress-strain curve is determined and the elastic moduli are calculated using **Eq. 7 and Eq. 8** below,

$$E = slope\ of\ the\ axial\ curve \quad \text{.....(7)}$$

$$\nu = -\frac{slope\ of\ the\ axial\ curve}{slope\ of\ the\ radial\ curve} = -\frac{E}{slope\ of\ the\ radial\ curve} \quad \text{.....(8)}$$

where E is Young's modulus in psi^{-1} and ν is Poisson's ratio. $slope\ of\ the\ axial\ curve$ is found from the straight-line portion on the plot of Axial Stress vs. Axial Strain while $slope\ of\ the\ radial\ curve$ is found from the straight-line portion on the plot of Axial Stress vs. Radial Strain. For consistency, the same stress ranges were used to determine both Young's modulus and Poisson's ratio for the same sample. An example interpretation for a castlegate sandstone sample is shown in **Figure 5** and **Figure 6**.

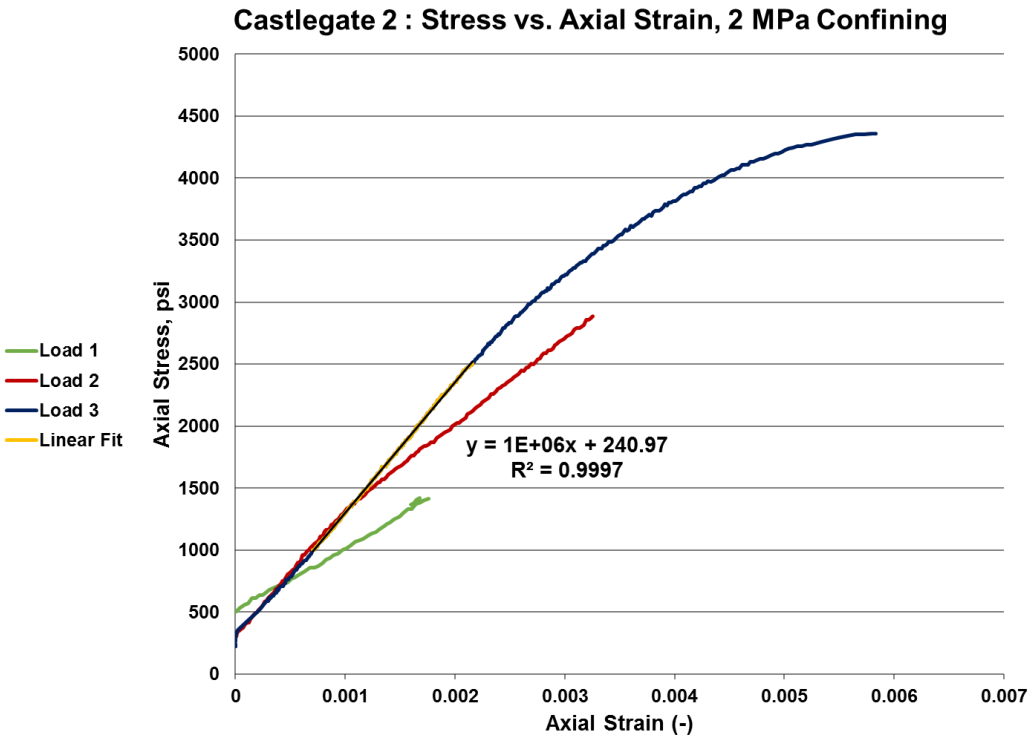

Figure 5-Example Axial Stress vs. Axial Strain curve used to determine Young's modulus.

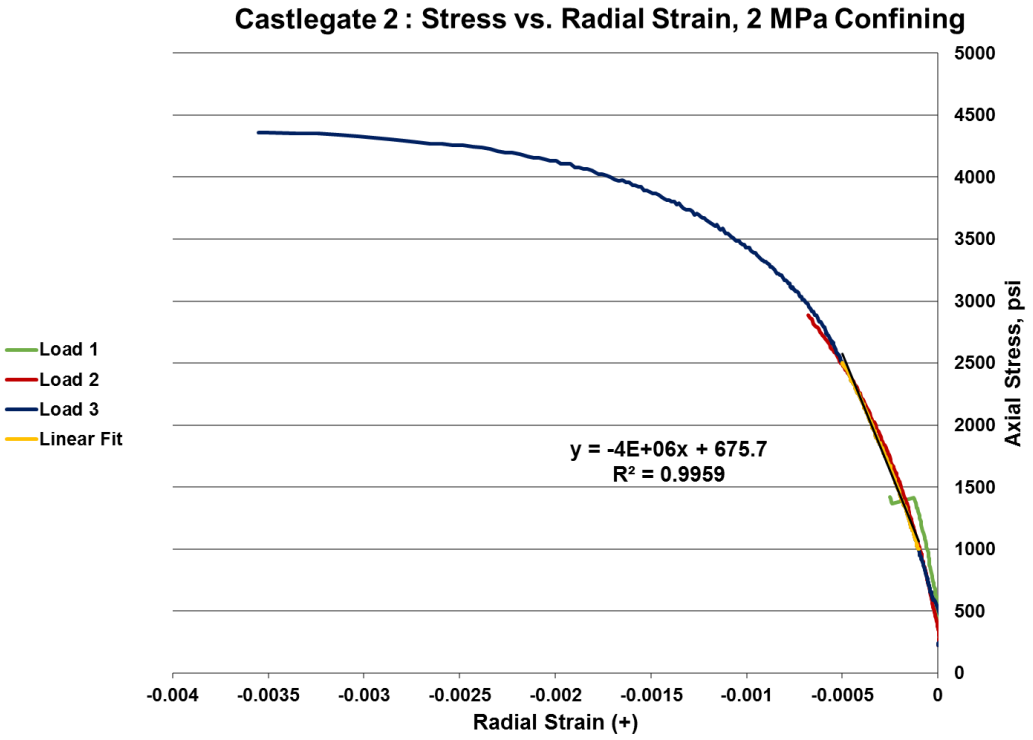

Figure 6-Example Axial Stress vs. Radial Strain curve used in the determination of Poisson's ratio.

Notice the straight-line portion of the third loading stage is used, where all inelastic deformation has been removed from the rock sample. Axial stress during the last loading stage was increased until sample failure to obtain a value for compressive strength.

2.4 Brinell Hardness

Brinell hardness is an indentation hardness test and its value is dependent on the diameter of an indentation on the rock's surface caused by a spherical indenter of known diameter, under a controlled vertical force. The test was conducted according to the Standard Test Method for Brinell Hardness of Metallic Materials, known as ASTM E10-

14. Each sample was tested using a tungsten carbide indenter of 1/8" diameter. Given that a ball indenter of this diameter was not listed in the standard, the two force/diameter ratios of 10 and 5 for a ball indenter with a diameter of 2.5 mm were used. Consequently, a force of 0.5 kN and 1 kN were applied in three separate locations along the sample surface. The indentation diameters were measured in two directions perpendicular to each other and subsequently averaged. The Brinell hardness value for each indentation was calculated and an average of all six indentations were used as the final value for each sample. Knorr (2016) presents a systematic procedure for conducting the test using the GCTS PLT-100 setup, pictured in **Figure 7**.

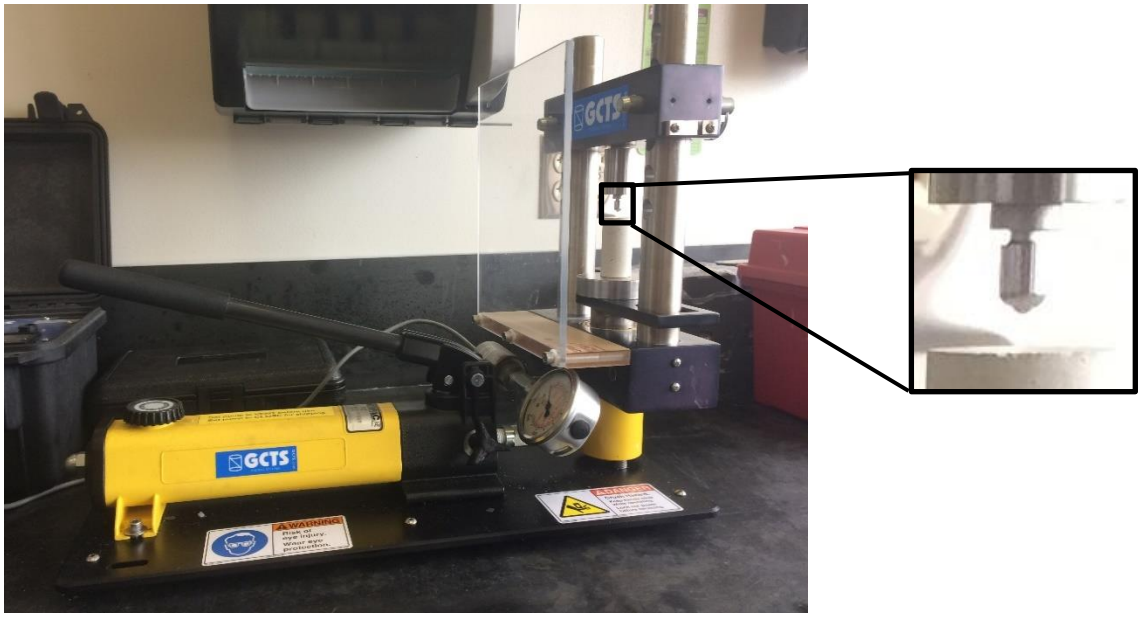

Figure 7-Apparatus for conducting the Brinell hardness test with zoomed in view of the spherical indenter.

The device used to measure the diameters of the induced indentations was the Newage® 5620 Series "HiLight" Brinell scope. Once the indentation diameters are measured, **Eq. 9** is used to calculate the actual Brinell hardness number, HBW.

$$HBW = \frac{2F_{kgf}}{\pi D(D-\sqrt{D^2-d^2})} \quad \text{.....(9)}$$

F_{kgf} is the test force in kgf, D is the diameter of the indenter ball in mm, and d is the measured mean diameter of the indentation in mm.

2.5 Mineralogy and Brittleness

Mineralogy of each shale outcrop was determined using X-ray powder diffraction (XRD) analysis. Samples were crushed into powder using an agate mortar and pestle set and required to pass through a 200-µm sieve. To compare mineralogy between formations, a brittleness index (**Eq. 10**) was used, defined simply as a volume fraction ratio of brittle minerals to the entire rock matrix.

$$BI = \frac{V_{Brittle}}{V_{Brittle}+V_{Non-Brittle}} \quad \text{.....(10)}$$

Quartz, dolomite, and pyrite were considered as the primary minerals that significantly contributed to the shale's brittleness.

2.6 Fracture Face Surface Characterization

Fracture surfaces of each shale conductivity sample were distinguished based on their surface roughness, measured using a laser profilometer. The profilometer apparatus along with a sample interpretation of results are shown in **Figure 8**.

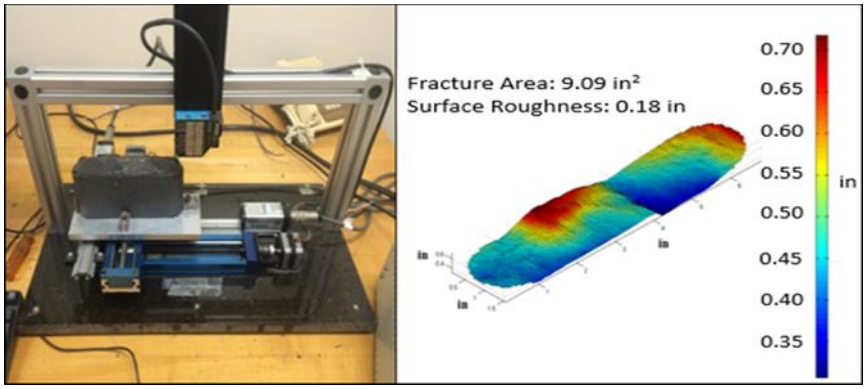

Figure 8-Surface laser profilometer apparatus and roughness results (reprinted from Enriquez-Tenorio et al. 2016).

Roughness (ε) was calculated with **Eq. 11**, following the root mean square method.

$$\varepsilon = \sqrt{\frac{1}{n}\sum_{i=1}^{n}(Z_i - \bar{Z})^2} \quad \text{.....(11)}$$

$\bar{Z}$ represents the average of all height readings across the fracture surface, whereas Z is the height reading at one of the n points. The device has a recordable height range of 1 inch, precise to 0.000001 inches. A grid size of 0.05 inches was used to sufficiently characterize the surface roughness.

2.7 Multiple Linear Regression

Multiple linear regression, also called ordinary least squares regression, is a statistical process which models a response (dependent) variable as a linear combination of a set of predictor (independent) variables. This process was chosen to examine the relationship between fracture conductivity and multiple experimental variables because of its ability to handle nonlinear relationships and the ease of interpretability when compared to other methods. Nonlinearity is handled by applying mathematical operations, such as the logarithm or square root, to transform the initial relationship between two variables into linearity. It is assumed in this regression technique that:

1. The response and predictor variables with transformations are linearly related.
2. The errors are independent of each other (e.g. random samples or randomized experiments) and normally distributed, with a mean of zero.
3. There is a constant variance among the residuals.

Assumptions are checked by plotting the residuals (the difference between the predicted and the measured values) against all variables and verifying error normality. All assumptions must be met to result in a valid model. It is also vital that two or more predictor variables not be highly correlated with each other (no collinearity). This is accomplished by mitigating the variance inflation factor of each predictor, which is a measure of how well that predictor is correlated with all other independent variables. The variance inflation factor (VIF) for each predictor is represented by **Eq. 12**.

$$VIF = \frac{1}{1-R^2} \quad \text{.....(12)}$$

R^2 in this case is the correlation coefficient when that particular predictor is regressed with all other independent variables. A variance inflation factor of less than five was considered acceptable in this study. To evaluate parameter significance, each independent variable is ranked based on the P-values from the hypothesis test. When a predictor variable does not correlate to the response variable, the slope of the plot of response versus predictor, β, is zero. This represents the null hypothesis. On the other hand, the alternative hypothesis is β is not equal to 0, meaning a significant relationship exists between the response and predictor variable. A P-value is essentially the probability that the null hypothesis is mistakenly rejected for the alternative. Therefore, a low P-value is a strong indication of correlation between two variables. A significance cutoff of .05 for the P-value is used in this study. It is important to mention that if the P-value is higher for one variable than another, it does not necessarily mean that variable has a higher association with the response. This is because P-values depend on correlation between predictors, the slope of the regression line, and sample size. For a response variable with multiple predictor parameters, a multiple linear regression prediction model has the general format of **Eq. 13**,

$$Y_i = \beta_0 + \beta_1 X_{1i} + \beta_2 X_{2i} \ldots \beta_k X_{ki} \quad \text{.....(13)}$$

where Y_i is the response variable, X_{ki} are multiple predictor variables, and β_i are the slopes representing the relationship between that specific predictor and response. Transformation and interaction terms are added to make the linear relationship presented by Eq. 13. It is important to mention an interaction between two input variables exists when the effect of one input (X_1) on the response variable (Y) is different for different values of the other input (X_2). For example, injecting one more pound of sand (X_1) into a hydraulically fractured well has a larger effect on production (Y) when the well is shorter (X_2). An interaction would be represented by $\beta_3 X_{1i} X_{2i}$ in Eq. 13.

3. SHALE FRACTURE CONDUCTIVITY CORRELATION*

This section presents the generation of shale fracture conductivity correlations utilizing past experimental data. The purpose of this robust statistical analysis is to predict shale fracture conductivity for various proppant loadings and rock properties under a range of closure stresses. A plethora of rock properties were measured throughout these experiments, therefore, it is advantageous to first divide the sample size into smaller subsets to identify key drivers in the overall model. With this in mind, the results are systematically presented in four subsets separated by the different formations. Variable distributions are shown for each set along with an ordinary least squares regression analysis and parameter significance ranking specific to that subset. Lastly, all data is combined for the overall correlation. The parameters that were varied in each set of experiments are summarized in **Table 2**. For example in the Barnett dataset, rock mechanical properties along with mineralogy and surface roughness were relatively constant between experiments while the effects of proppant size, concentration, and closure stress were analyzed.

* Reprinted with permission from "A Comparative Analysis of Rock Properties and Fracture Conductivity in Shale Plays" by Cody Kainer, Dante Guerra, Ding Zhu, and Alfred D. Hill, 2017. Copyright 2017 by Society of Petroleum Engineers.

Table 2-The parameters varied in each set of experiments for the different shale formations.

Formation	Closure Stress	Young's Modulus	Poisson's Ratio	Brinell Hardness	Mineralogy	Proppant Size	Proppant Concentration	Surface Roughness
Barnett	•					•	•	
Fayetteville	•	•	•		•	•	•	
Marcellus	•	•	•		•		•	•
Eagle Ford	•	•	•	•	•	•		•

All specimens used for testing were collected from outcrops of their respective formation. In every instance, care was taken to acquire samples deep within the face of the outcrop, less affected by weathering and humidity.

3.1 Barnett Shale

The Barnett Shale formation is located in the Fort Worth Basin and tends to thin out moving south towards the Llano Uplift. A rock quarry located in this general area near the southwest tip of the formation is where the Barnett outcrop samples were collected for this study. The Barnett dataset focused primarily on the effects of varying proppant size and proppant concentration. All samples were fractured along the bedding plane, which resulted in relatively flat faces with little asperity. Differences in elastic moduli, Brinell hardness, and mineralogy between specimens were also deemed negligible as all rocks were collected in the same location and fractured in the same orientation. These parameters were examined in the study; proppant size, concentration, and closure stress. 55 individual conductivity tests are included. The distributions of the three experimental variables for the Barnett shale samples are shown in **Figure 9**. In this figure

and subsequent figures, "Count" refers to the number of data points included in the model at each condition.

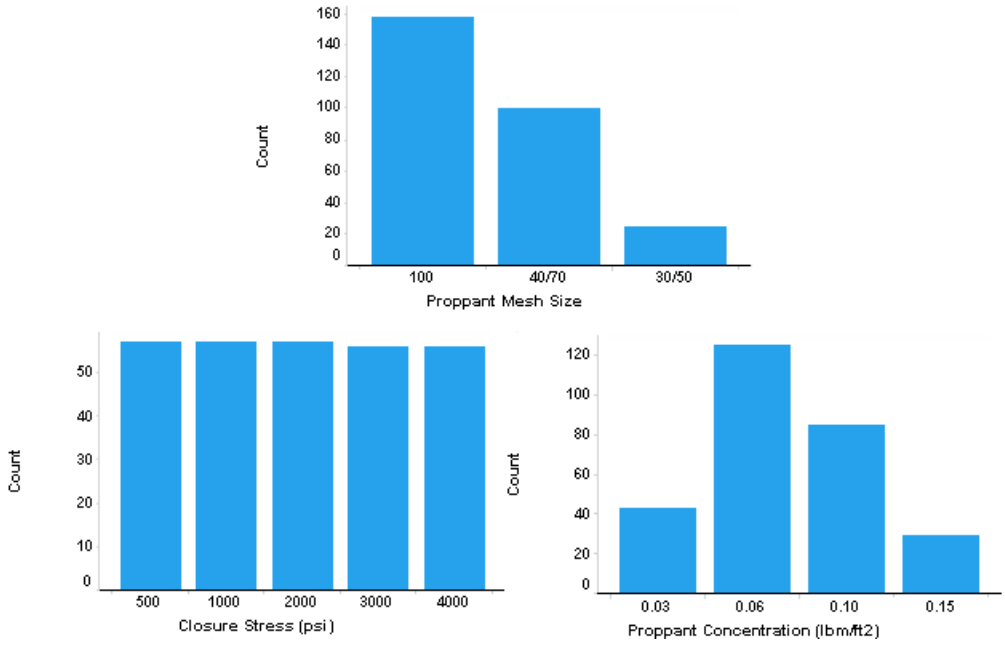

Figure 9-Distribution of Barnett experimental conductivity data.

All conductivity tests experienced closure stresses ranging from 500 to 4,000 psi. A broad range of proppant concentrations and mesh sizes were tested with a statistically significant amount of observations at each condition. The proppant sizes used were 30/50, 40/70, and 100 mesh. The proppant concentration varied from 0.03 to 0.15 lbm/ft^2 of "Northern White" sand from Wisconsin. The distribution of measured fracture conductivity as an overall response to the independent variables is displayed in **Figure 10**. Barnett conductivity ranged from 5 to 1700 md-ft with a log normal distribution. The majority of the values were in the 5 md-ft to 50 md-ft range.

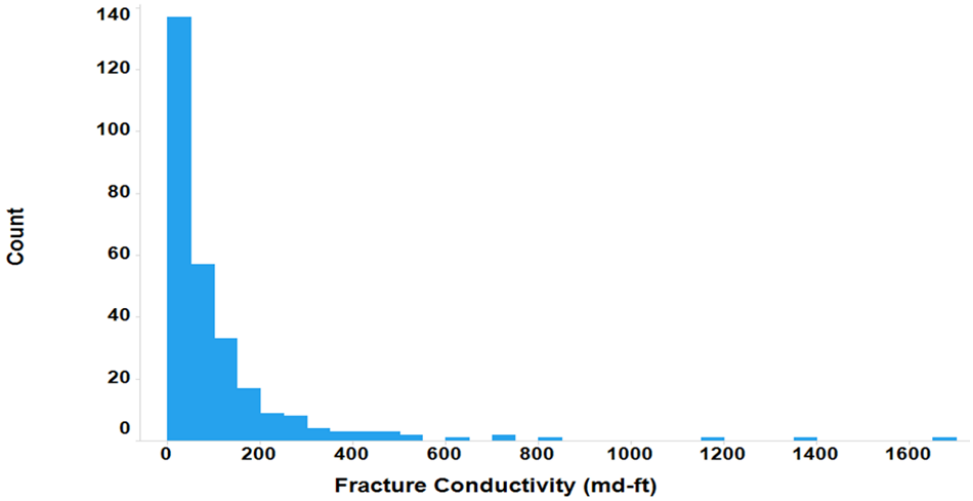

Figure 10-Barnett fracture conductivity distribution.

The ordinary least squares regression technique was applied to the sample set to obtain a best-fit equation (**Eq. 14**) as:

$$\ln(C_f) = 5.97 - .00065\sigma_c + 9.90C_p + \beta_3, \qquad \beta_3 = \begin{cases} -1.07\ for\ 100\ mesh \\ 0.008\ for \frac{40}{70}\ mesh \\ 1.06\ for \frac{30}{50} mesh \end{cases} \quad \text{.....(14)}$$

The equation-predicted conductivity is plotted against the measured conductivity, as displayed in **Figure 11**. A perfect prediction would show actual and predicted values overlaying each other, with a slope of one. The logarithm transformation was applied to conductivity because the conductivity declines exponentially with closure stress.

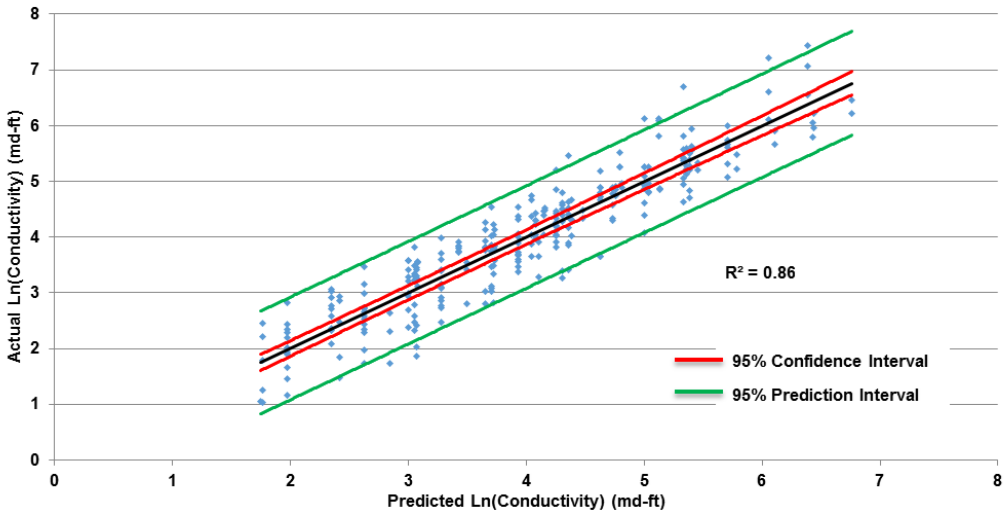

Figure 11-Barnett conductivity model results showing actual vs. predicted values.

Displayed on Figure 11, the red and green lines represent 95% confidence and prediction intervals respectively. For a given set of predictors, the confidence interval essentially says there is a 95% probability the mean of the predicted response values from the model would fall between the red lines. The prediction interval is concerned with predicting individual responses as opposed to the mean. Therefore, it is inherently always wider than the confidence interval. This procedure also provides insight into which parameters are dominating conductivity behavior. **Figure 12** ranks the most statistically significant parameters based on their P-values. The definition of a P-value was explained in the "Multiple Linear Regression" section.

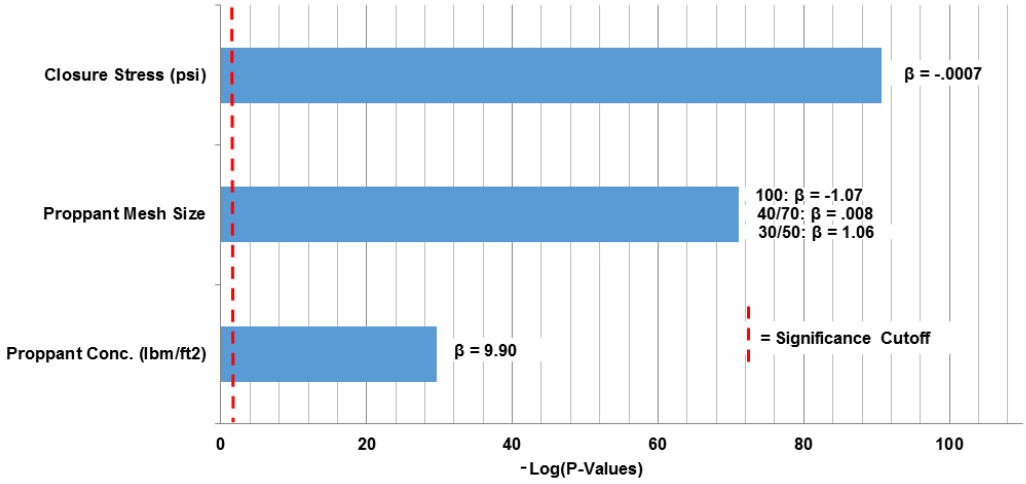

Figure 12-Influential parameters on conductivity for the Barnett sample set.

The red dashed line indicates the 0.05 cutoff for the minimum P-value required for significance. As expected, closure stress dominates conductivity behavior followed by proppant mesh size and concentration. Because no rock properties were varied, the only variables that showed to be influential were related to the proppant and sample loading conditions. β values indicate that conductivity decreases with closure stress (negative slope), and increases with proppant mesh size and concentration (positive slope). The Barnett Shale test data was excellent proof of a valid experimental set up and procedure, but was not robust enough to examine the effects of rock and fracture properties on conductivity.

3.2 Fayetteville Shale

The Fayetteville shale is divided into three primary zones deemed the Upper, Middle, and Lower Fayetteville. The Lower Fayetteville can further be divided in the LFAY, FL2, and FL3, as discussed by Harpel et al. (2012). The Fayetteville outcrop

samples used in the study were taken from both the FL2 and FL3 layers, which are normally targeted for completion. The Fayetteville tests involved varying proppant conditions, and in addition, different mechanical properties and mineralogy between the FL2 and FL3 layers. Values of Young's modulus and Poisson's ratio were attributed to each of the two layers from triaxial tests. Mineralogy was determined for each conductivity set in the original data from which specific values of brittleness index could be calculated for each test. Distributions for all experimental variables are shown in **Figure 13**, containing 23 individual tests. Three different proppant sizes of 100, 30/70, and 40/70 mesh of Arkansas River sand were used at concentrations of 0.03 to 0.5 lbm/ft^2. Only a few data points were obtained at 4,000 psi closure stress due to the rock's fragility and brittleness under load. Surface roughness of each layer was also measured on selected samples only. **Figure 14** shows the distribution of conductivity values for the Fayetteville samples. The range was similar to the Barnett samples with a maximum value around 2200 md-ft and most of the measurements between 8 md-ft to 50 md-ft. A correlation equation (**Eq. 15**) was obtained analogous to that of the Barnett presented earlier (Eq. 14). **Figure 15** shows the results from the correlation for the Fayetteville samples.

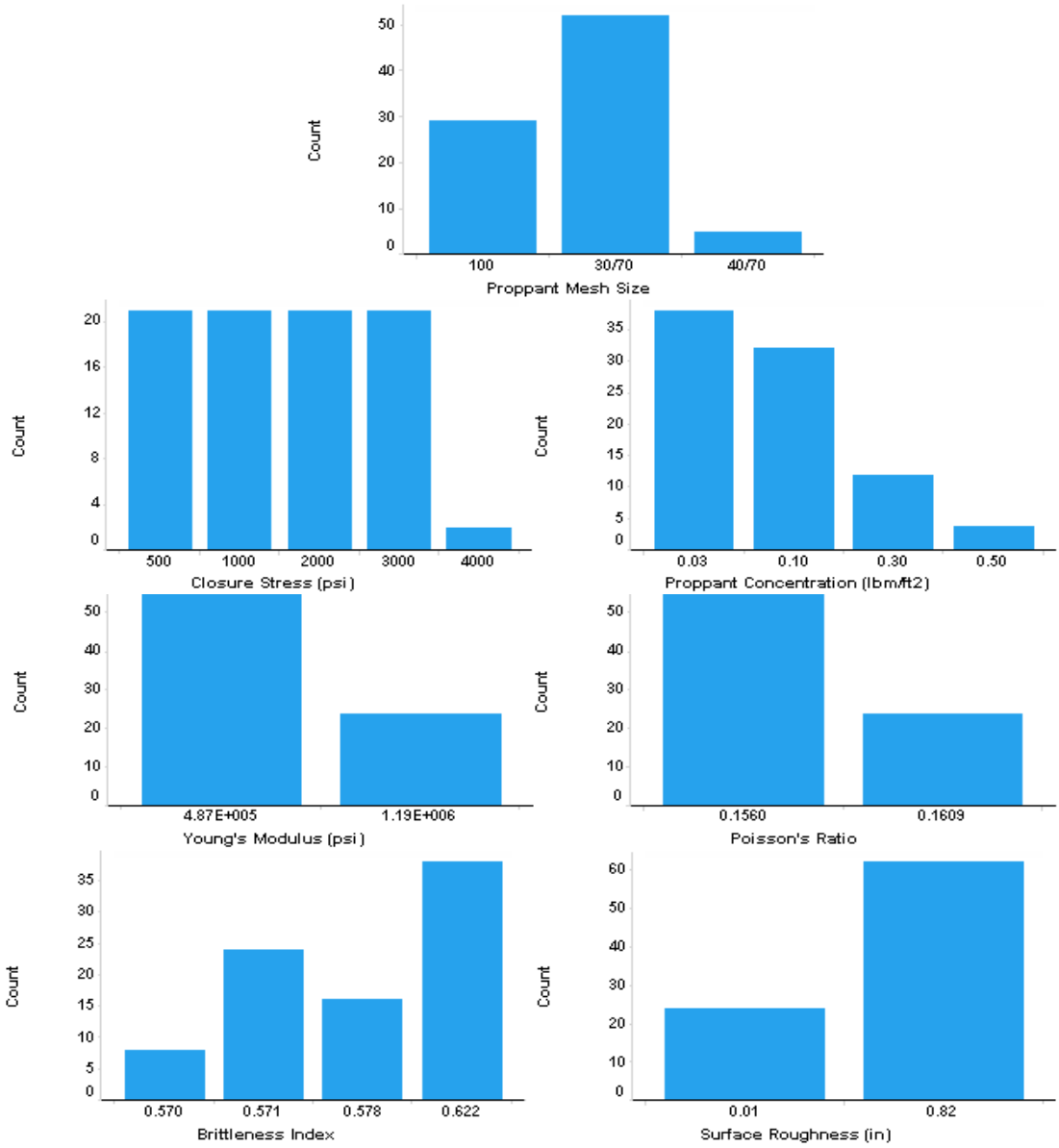

Figure 13-Distributions of Fayetteville experimental conductivity data.

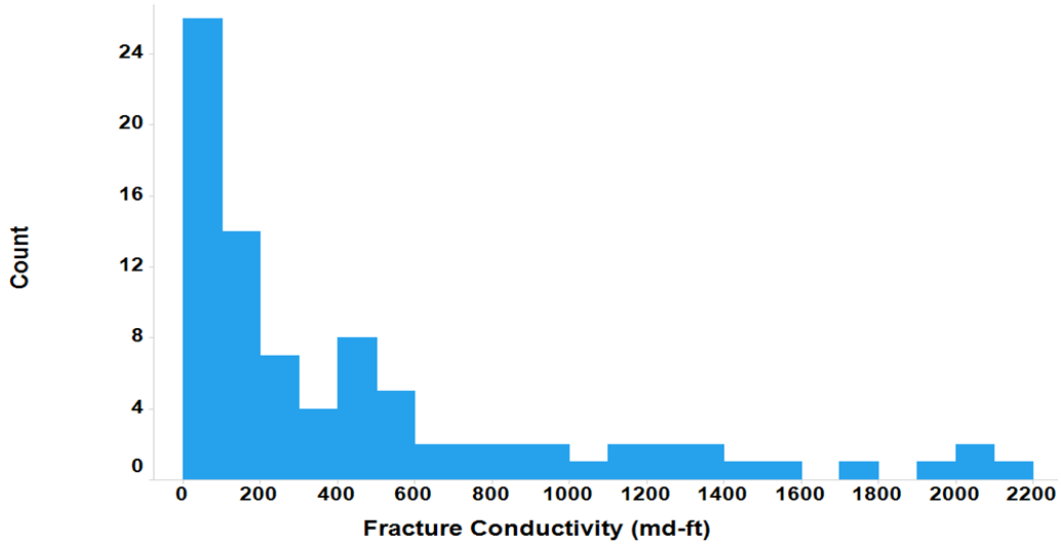

Figure 14-Fayetteville fracture conductivity distribution.

$$\ln(C_f) = -15.80 - .00075\sigma_c + 2.92C_p + 38.61BI + \beta_4,\ \beta_4 = \begin{cases} -1.37\ for\ 100\ mesh \\ 0.849\ for \frac{30}{70}\ mesh \\ .518\ for \frac{40}{70} mesh \end{cases} \quad \ldots.(15)$$

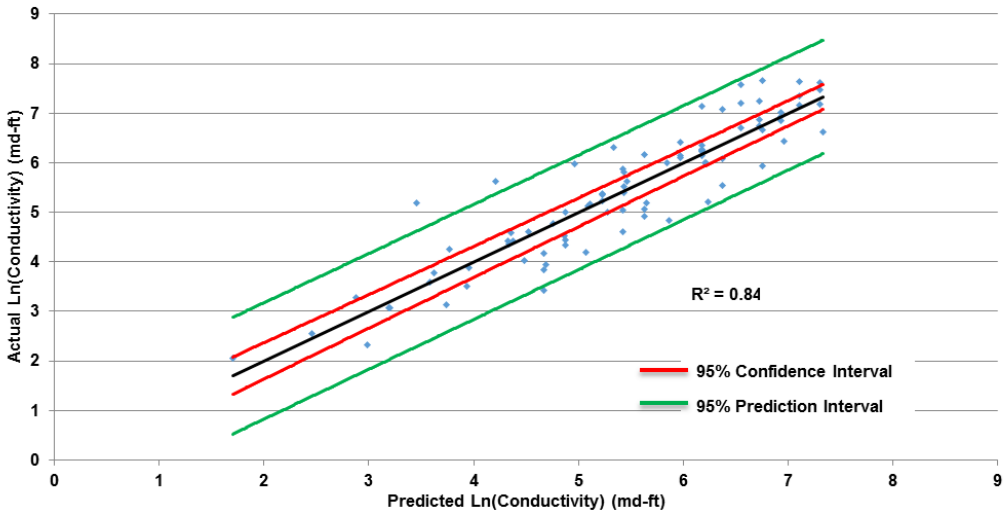

Figure 15-Fayetteville conductivity model results showing actual vs. predicted values from the model.

An excellent match was obtained once again by applying the logarithm transformation to conductivity. The confidence interval is slightly larger when compared to the Barnett sample results due to the smaller sample size for this data set. Proppant mesh size, concentration, closure stress, and brittleness index were all shown to have significant relationships with conductivity (**Figure 16**).

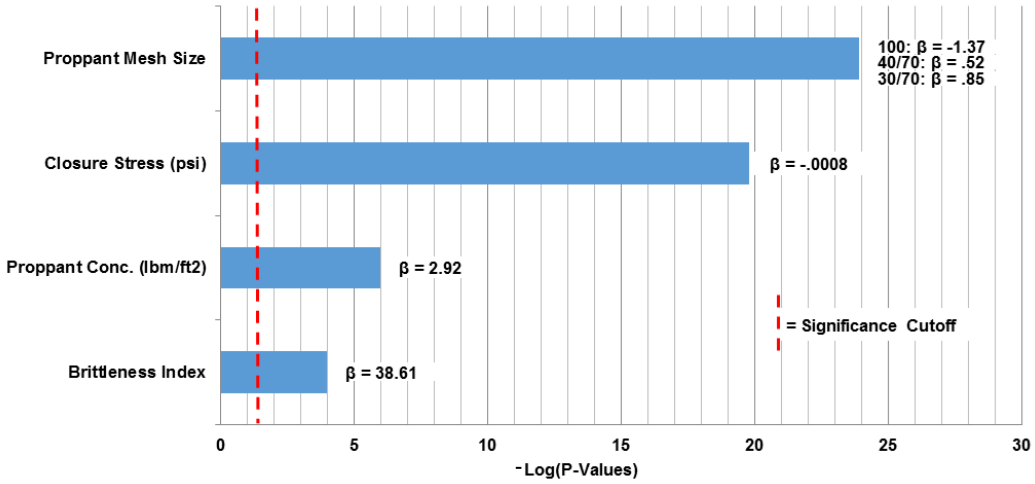

Figure 16-Influential parameters on conductivity for the Fayetteville sample set.

Young's modulus, Poisson's ratio, and surface roughness did not appear to be significant simply due to the limited variability in measurements. Only two values for each of these parameters were available to be inputted into the model. Therefore, any one of these three parameters could have explained the same behavior in conductivity, and the solution would not have been unique. Figure 16 shows proppant mesh size as the strongest predictor, but this should be observed with caution. The small number of data points associated with the 40/70 mesh proppant is the reason why this P-value is so high. Nevertheless, it is still a strong predictor of conductivity. According to the β values,

conductivity decreases with increasing closure stress and increases with larger proppant mesh size, increased proppant concentration, and a higher brittleness index.

3.3 Marcellus Shale

Marcellus samples were collected in two different locations in Elimsport and Allenwood, Pennsylvania, separated by approximately ten miles. X-Ray Diffraction results showed similar mineralogy between the two locations and agreed with values found in the literature for the Marcellus. The Elimsport samples were more weathered than the Allenwood samples. The Marcellus data set was much more comprehensive in terms of rock mechanical properties and fracture surface characterization when compared to the Barnett and Fayetteville data and includes 40 individual conductivity tests. The same mesh size was used for all tests and the conductivity sets were taken to much higher closure stresses up to 6,000 psi, where the effects of mechanical properties become more evident. The varying values of Young's modulus and Poisson's ratio are due to the mechanical anisotropy present in the Marcellus shale. Conductivity and triaxial tests were run at two different orientations, one parallel and the other perpendicular to the primary bedding plane. This was done to account for the anisotropy and acquire a better range of properties. **Figure 17** shows the distributions of all dependent variables for the Marcellus sample set.

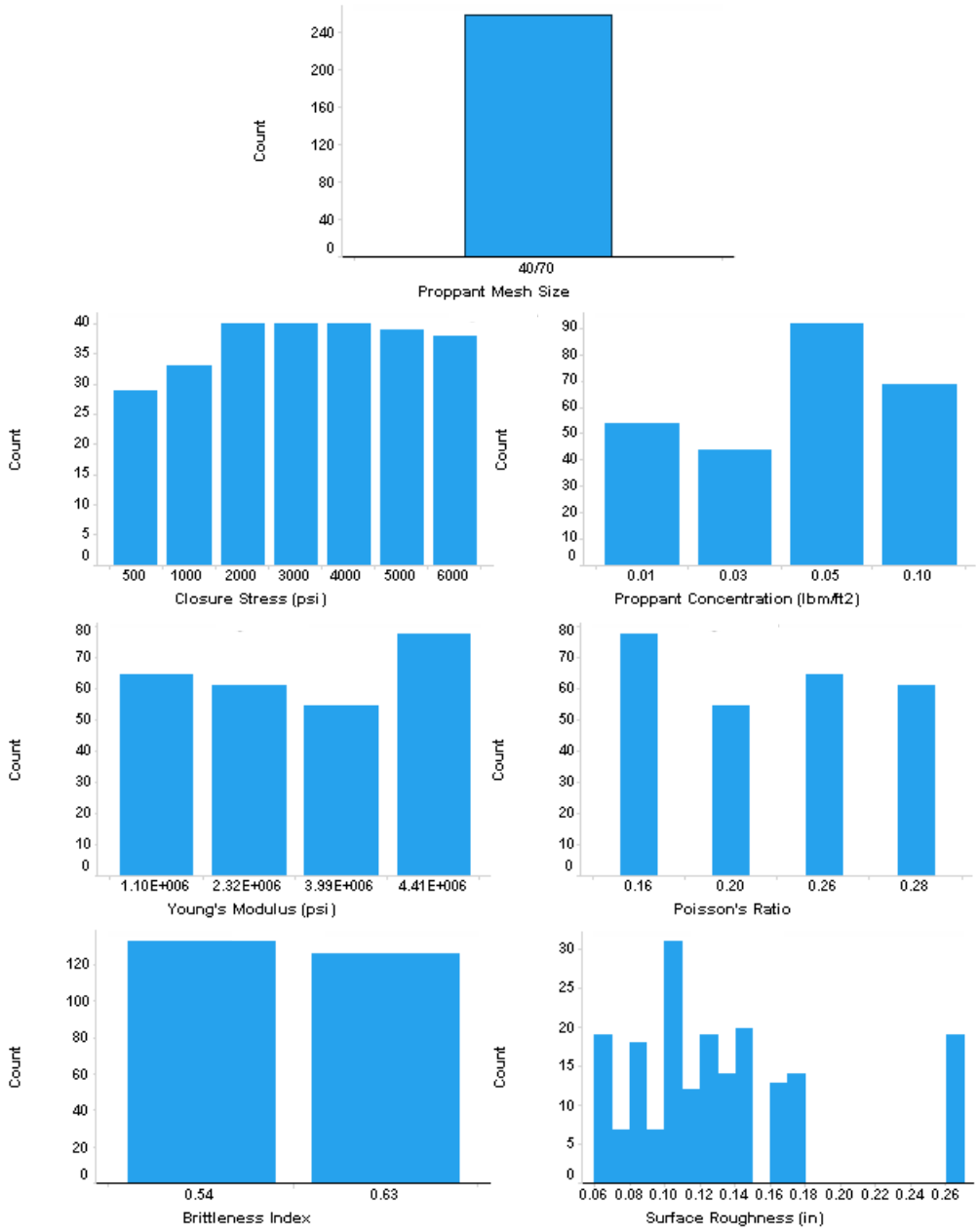

Figure 17-Distributions of Marcellus experimental conductivity data.

Young's modulus and Poisson's ratio ranged from $1.10x10^6$ to $4.41x10^6$ psi and .16 to .28 respectively. Proppant concentration was varied from 0.01 to 0.1 lbm/ft^2 at a mesh size

of 40/70. Proppant type was the same "Northern White" sand used in the Barnett conductivity tests. Fracture surfaces were relatively flat with roughnesses primarily between 0.06 and 0.18 inches. **Figure 18** plots the distribution of fracture conductivity measurements for the Marcellus experiments. Values were log-normally distributed with a broad range from 5 md-ft to nearly 6,000 md-ft.

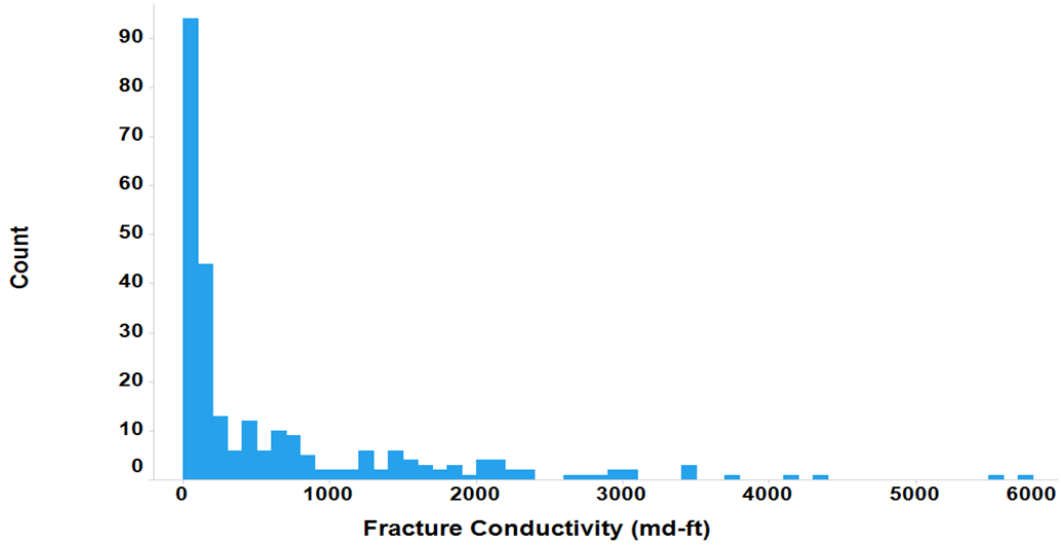

Figure 18-Marcellus fracture conductivity distribution

The results of the predicted conductivity using multiple linear regression (**Eq. 16**) against measured conductivity are displayed in **Figure 19**. In this case, the prediction interval is relatively wider due to the higher variations in the data, but the model still provides valuable insight on which parameters are affecting fracture conductivity.

$$\ln(C_f) = 3.99 - .000705\sigma_c + 8.76 \times 10^{-7}E + 30.76C_p - 4.55\varepsilon \quad \text{.....(16)}$$

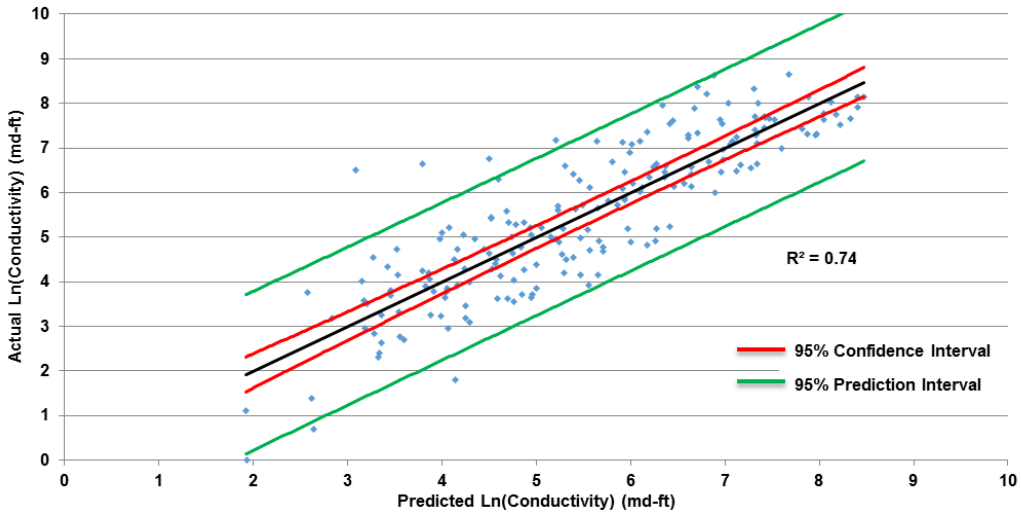

Figure 19-Marcellus conductivity model results showing actual vs. predicted values.

Variable significance is ranked based on their respective P-values and summarized in **Figure 20**, along with values for each β. Proppant mesh size does not appear significant in this case because as mentioned earlier, a single mesh size of 40/70 was used throughout all experiments.

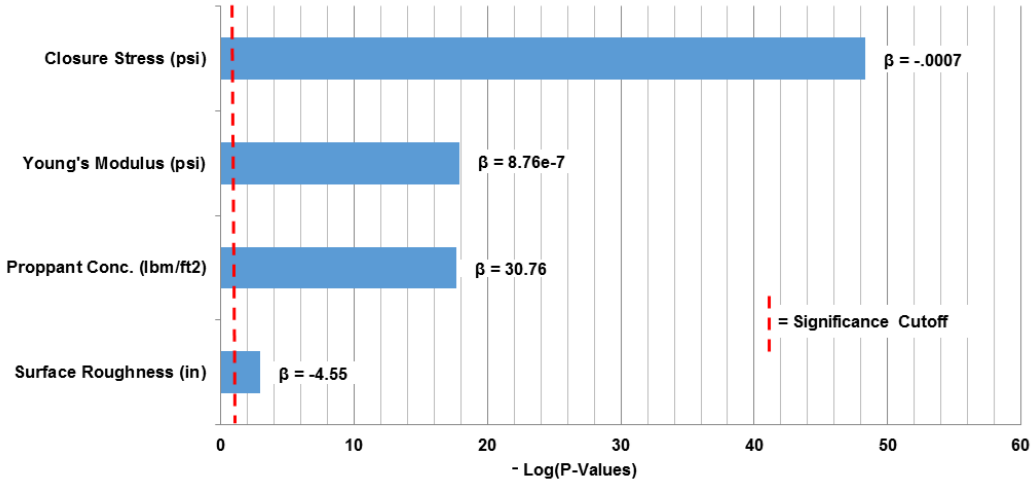

Figure 20-Influential parameters on conductivity for the Marcellus sample set.

Similar results are obtained as we observed in the other shale samples that closure stress and proppant concentration are the key drivers in the conductivity behavior. However, Young's modulus and surface roughness were also found to be influential. According to the positive β coefficient, a higher modulus resulted in higher conductivity values overall. Surface roughness was significant in this case due to the lower proppant concentrations of 0.01 lb/ft^2. These values are within the proppant monolayer range where surface asperities can create pinch points in the fracture as well as tortuous flow paths, which inhibit conductivity. This agrees well with a β value of -4.55 for surface roughness, exhibiting an inverse relationship with conductivity. Poisson's ratio was found to have no statistically valid effect on fracture flow performance. Interaction terms between Young's modulus, surface roughness, and proppant concentration were also investigated but none were found to be statistically significant.

3.4 Eagle Ford Shale

The Eagle Ford shale has five facies, A, B, C, D, and E. Some of the facies are further divided into sub facies as defined by Donovan et al. (2012). The Eagle Ford rock samples for this study were collected in Lozier canyon and Antonio creek, located in southwest Texas near the city of Langtry. All facies of the Eagle Ford shale (A, B, C, D, and E) were procured with emphasis placed on the high total organic content layer B. This dataset was the most robust compared to the other three shale formations. Each of the five sub facies of the Eagle Ford Shale had different mineralogical compositions as well as mechanical properties. As in the Marcellus data set, varying fracture orientations were also investigated, adding even more variability in the rock properties. Proppant

concentration was held constant at 0.1 lb/ft^2 throughout the experiments and mesh size was varied between 30/50 and 100 mesh of brown "Brady" sand. All distributions of the independent variables are displayed in **Figure 21-Distributions** of Eagle Ford experimental conductivity data.. Conductivity data for the 35 conductivity tests is shown in **Figure 22,** with a log normal distribution up to 12,000 md-ft.

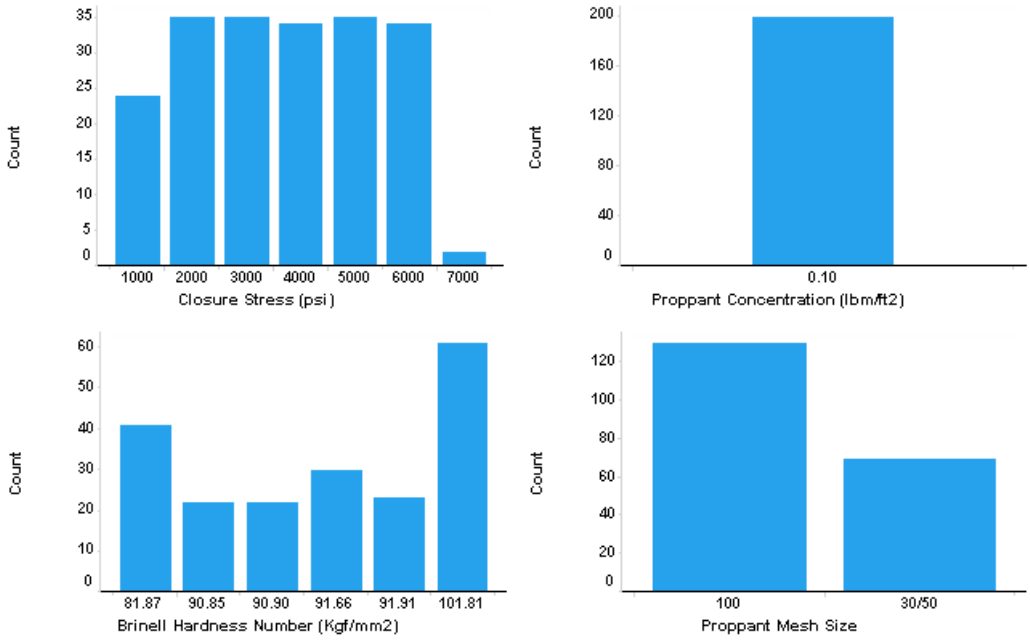

Figure 21-Distributions of Eagle Ford experimental conductivity data.

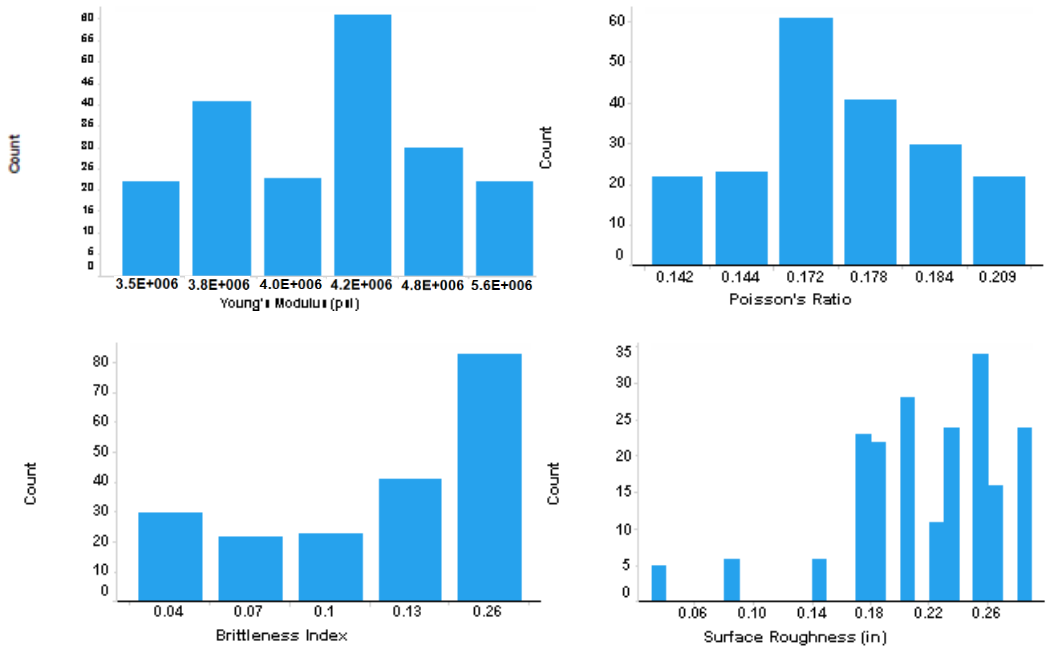

Figure 21 Continued-Distributions of Eagle Ford experimental conductivity data.

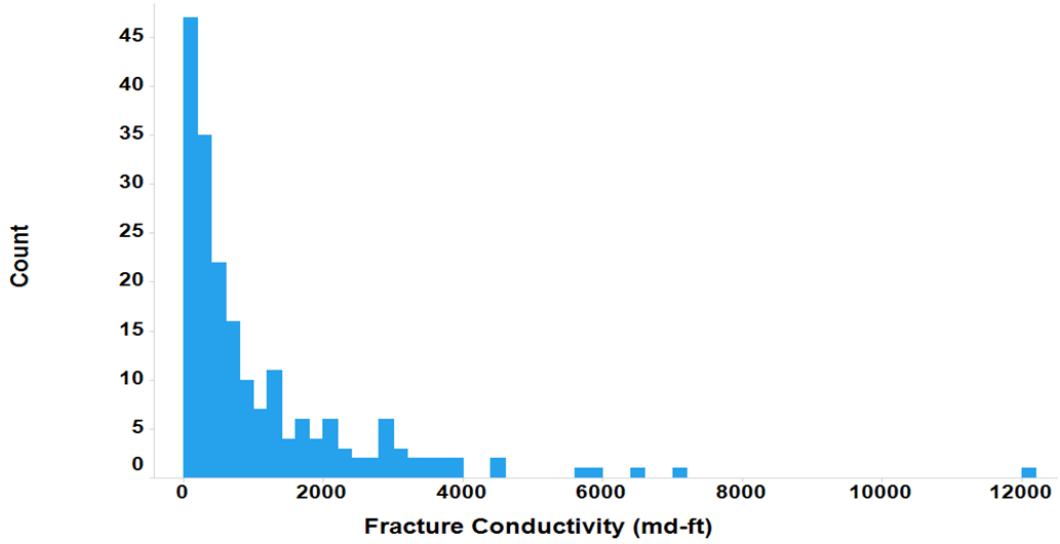

Figure 22-Eagle Ford fracture conductivity distribution.

The logarithm transformation was applied to conductivity and ordinary least squares regression was conducted (**Eq. 17**). The results of actual conductivity versus predicted

conductivity are shown in **Figure 23**. A relatively strong correlation was obtained, with constant variance from the regression line across all values of the response variable.

$$\ln(C_f) = 8.51 - .00061\sigma_c + .024BHN - 1.76BI - 10.48v + \beta_5, \qquad \beta_5 = \begin{cases} -.331 \; for \; 100 \; mesh \\ .331 \; for \; \frac{30}{50} \; mesh \end{cases} \quad (17)$$

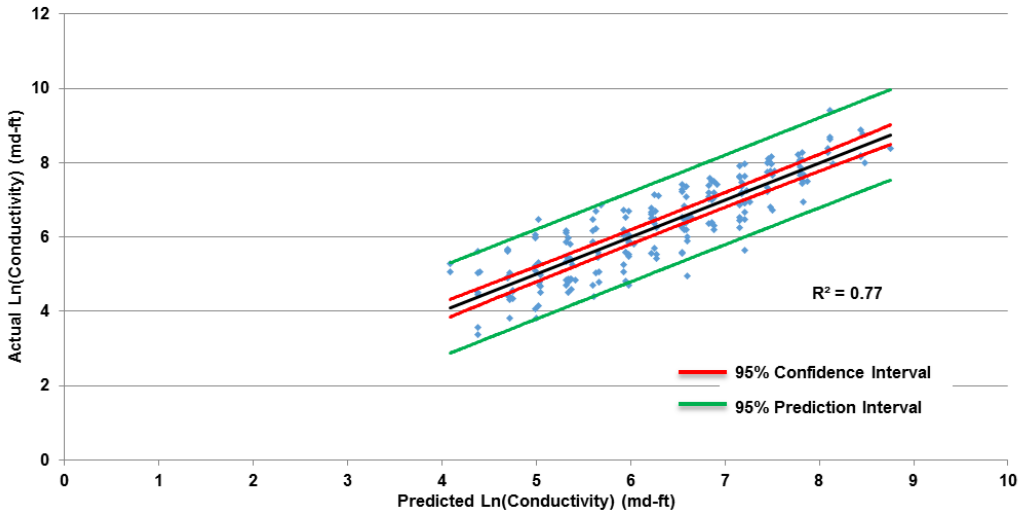

Figure 23-Eagle Ford conductivity model results showing actual vs. predicted values.

Parameters were then ranked based on their P-values from the model and summarized in **Figure 24**. Closure stress was the primary driver behind the change in conductivity followed by proppant mesh size, Poisson's ratio, Brinell hardness number, and the brittleness index. Proppant concentration is not shown here because this value was not varied in this set of experiments, as stated earlier.

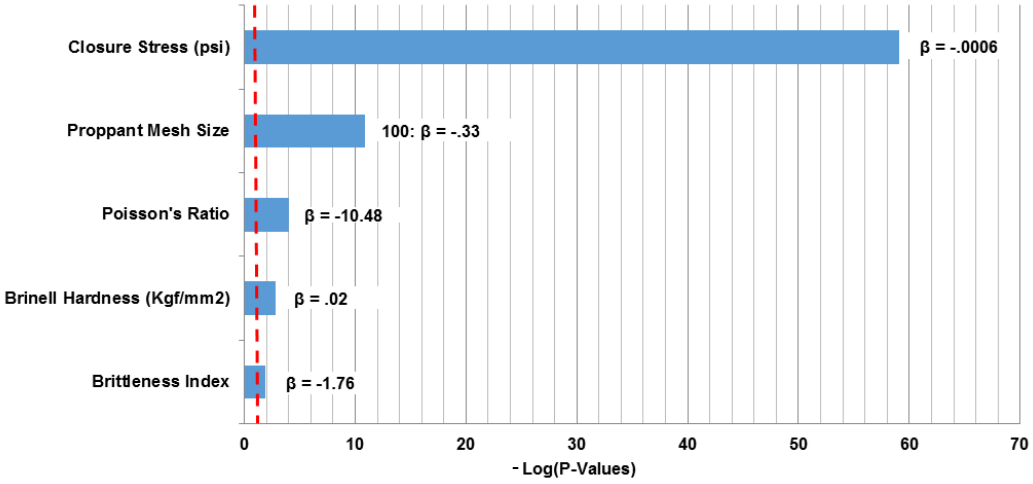

Figure 24-Influential parameters on conductivity for the Eagle Ford sample set.

The effect of proppant mesh size agreed well with what was observed in the other formations as conductivity increases with larger proppant. However, Poisson's ratio showed a significant impact with a negative relationship to conductivity, opposite to what was observed on Young's modulus in the Marcellus sample set. This could be attributed to the fact that collinearity existed within the data between Young's modulus, Poisson's ratio and Brinell hardness. Nevertheless, even with the linearly related predictors removed from the model, Poisson's ratio still proved to be a much more significant predictor of conductivity than Young's modulus. Brinell hardness was found to have a positive relationship with conductivity. A rock with higher Brinell hardness is generally less susceptible to proppant embedment as closure stress increases, which leads to a smaller reduction in fracture aperture, and ultimately conductivity. Even though it has been shown a power law relationship exists between embedment depth and Brinell hardness, the log transformation was not applied in this case. This was because the hardness values were

relatively high and covered such a small range, therefore, the relationship with conductivity appeared linear and resulted in a better fit.

3.5 Overall Prediction Correlation

Data from the Fayetteville, Marcellus, and Eagle Ford conductivity tests were combined to generate a correlation of fracture conductivity to various proppant conditions and rock mechanical properties. This was accomplished using the same linear regression technique but on combined data sets of the three formations. The Barnett sample set was essentially a study on proppant effects and did not include any rock properties. Therefore, it was excluded from contributing to this correlation. Proppant bulk density and initial proppant pack permeability instead of proppant type and mesh size were used as drivers for the model in an effort to make the correlation more encompassing to other proppant types. Proppant permeability at zero stress was estimated using the correlation presented in Barree et al. (2016). The correlation equation (**Eq. 18**) based on all valid data is:

$$\ln(C_f) = 6.82 - .000686\sigma_c + 1.258\ln(E) + .01\,K_0 - .191\rho_{bulk} + 7.45C_p \quad \text{.....(18)}$$

This correlation of fracture conductivity, C_f, includes as variables, the effective fracture closure stress, σ_c, Young's modulus, E, proppant permeability at zero stress, k_0, proppant bulk density, ρ_{bulk}, and proppant concentration, C_p. The predicted conductivity is plotted against the measured conductivity, shown in **Figure 25**, with a satisfactory fit. **Figure 26** shows the variable significance ranking.

The correlation presented here is based on an extensive experimental study and careful statistical regression analysis. The independent variables' impacts on conductivity are confirmed with physical explanations. The correlation also ranks the importance of major parameters on conductivity behavior. This can be used as a reference to design proppant conditions based on formation properties and to estimate the resultant conductivity of a fracture job.

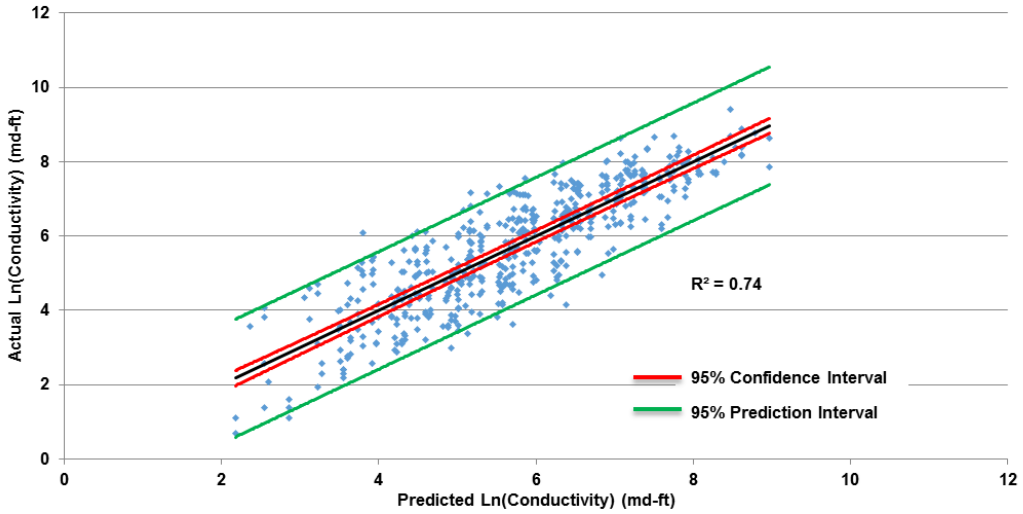

Figure 25-Combined data set model results showing actual vs. predicted values.

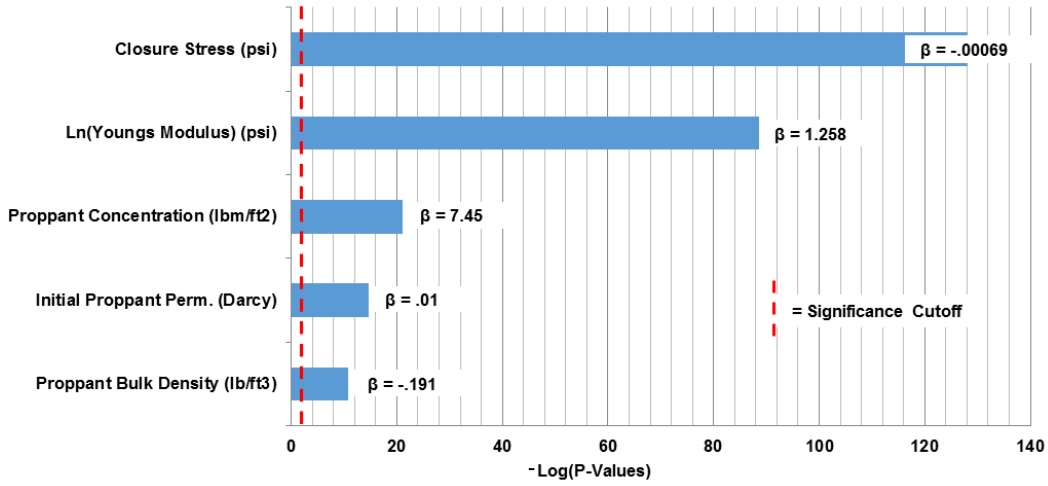

Figure 26-Influential parameters on conductivity for the combined data set.

The log transformation applied to Young's modulus in the final model resulted in a better fit because a broader range of values was available and the power law relationship between modulus and conductivity loss was more evident. This relationship is likely due to Young's modulus being correlated with another mechanical property concerned with inelastic stress-strain behavior. Poisson's ratio and Young's modulus were the only two mechanical properties available across the three shale formations to include in the model.

4. EXPERIMENTAL RESULTS AND DISCUSSION OF ROCK MECHANICS EFFECTS ON FRACTURE CONDUCTIVITY

Even though mechanical properties were varied in the shale conductivity experiments, many other variables were present which made it difficult to pinpoint the effects each property was having on conductivity. In addition, there were significant gaps in the data where important mechanical properties were not measured for certain formations. For example, Brinell hardness was only measured for the Eagle Ford dataset and compressive strength only for the Marcellus samples. This section presents results from a new rock mechanics study, which isolated the properties of Brinell hardness, Young's Modulus, Poisson's ratio, and compressive strength. The relationship between these parameters and fracture conductivity is discussed along with validation for how these properties should be handled in the conductivity correlations. The four formations investigated were Austin chalk, Lueders limestone, Crab Orchard sandstone, and Castlegate sandstone. These rocks were readily available and offered a wide range of mechanical properties, which were the primary concerns in sample selection.

4.1 Fracture Conductivity Results

Three conductivity samples from each formation were initially obtained for testing. Due to difficulties with hydraulic pump failures and premature sample failure, 9 of the 12 tests were ran successfully and are presented here. Each conductivity curve is shown on a semi-log graph, with closure stress on the x-axis ranging from 0 to 8,000 psi.

Exponential fits are applied to each curve (straight-line on semi-log) and the R-squared values are shown. As a reminder, all tests used the same 30/50 mesh ceramic proppant at a concentration of .3 lb/ft^2 on milled fracture surfaces. Results for individual conductivity tests are shown in **Figures 27-30**, with respect to formation type.

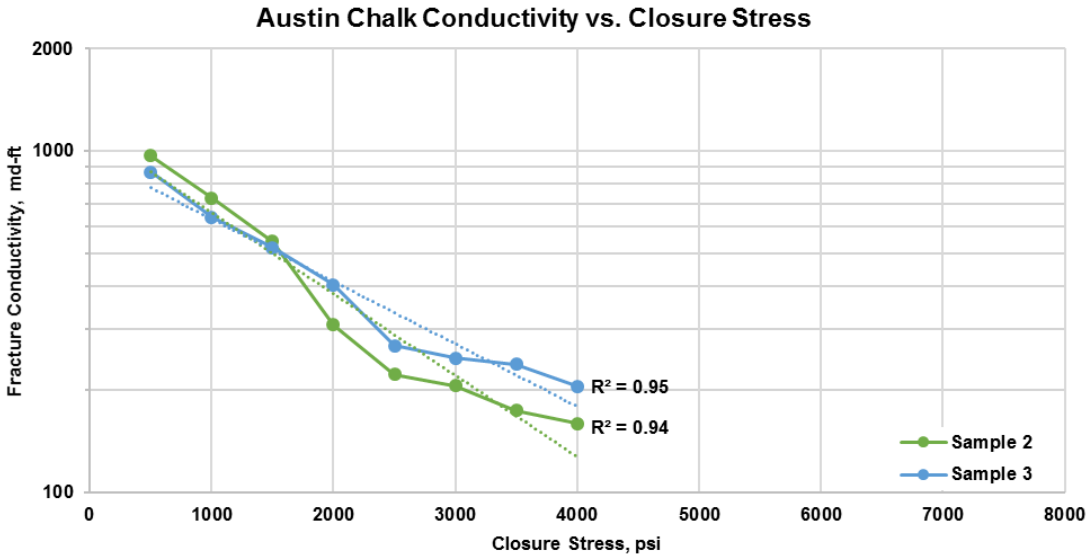

Figure 27-Austin chalk conductivity results.

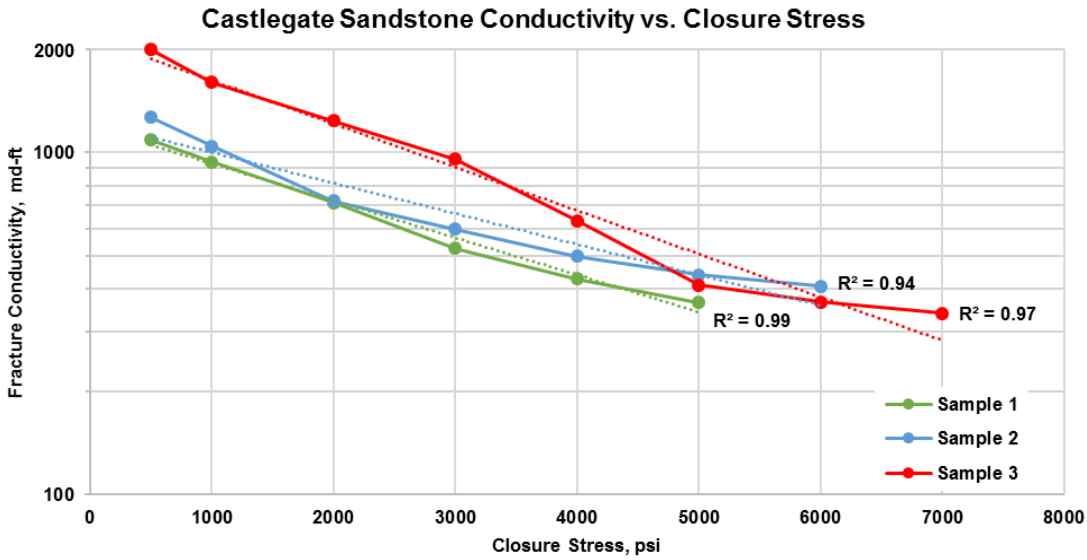

Figure 28-Castlegate sandstone conductivity results.

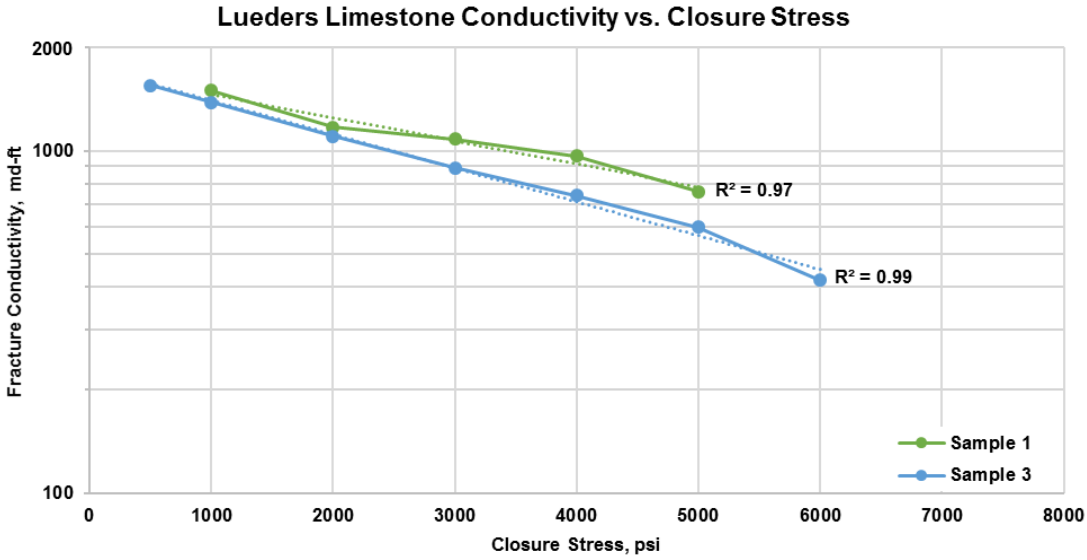

Figure 29-Lueders limestone conductivity results.

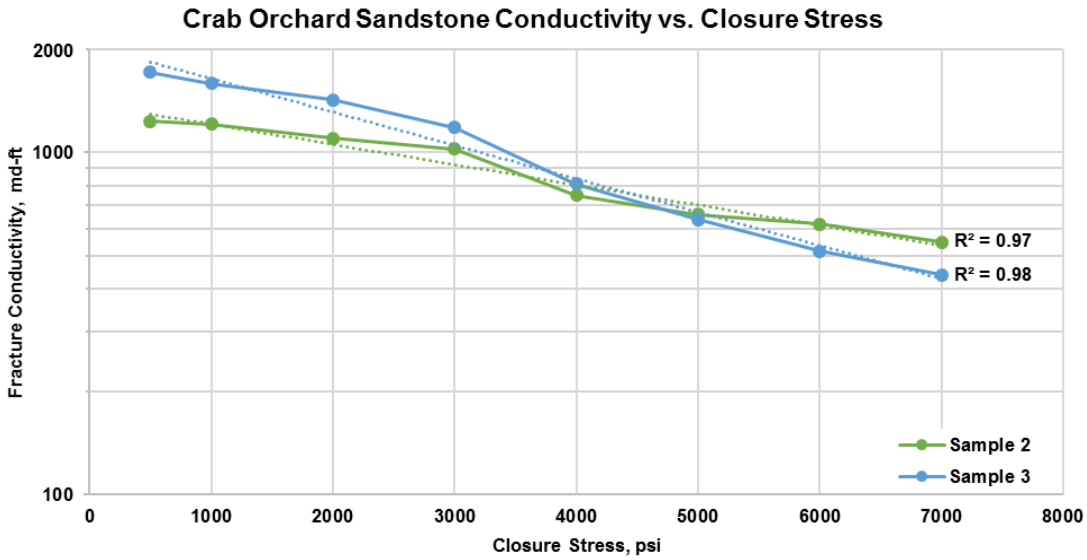

Figure 30-Crab Orchard sandstone conductivity results.

Overall, results were highly repeatable between tests for the same rock type. Small variations in initial conductivity values at lower closure stresses were likely due to slight differences in the initial proppant distribution inside the fracture. However, the decline of conductivity from this initial value was mostly consistent for the same rock type. **Figure 31** summarizes these results on the same plot for easier cross comparison, with average conductivity values at each closure stress presented.

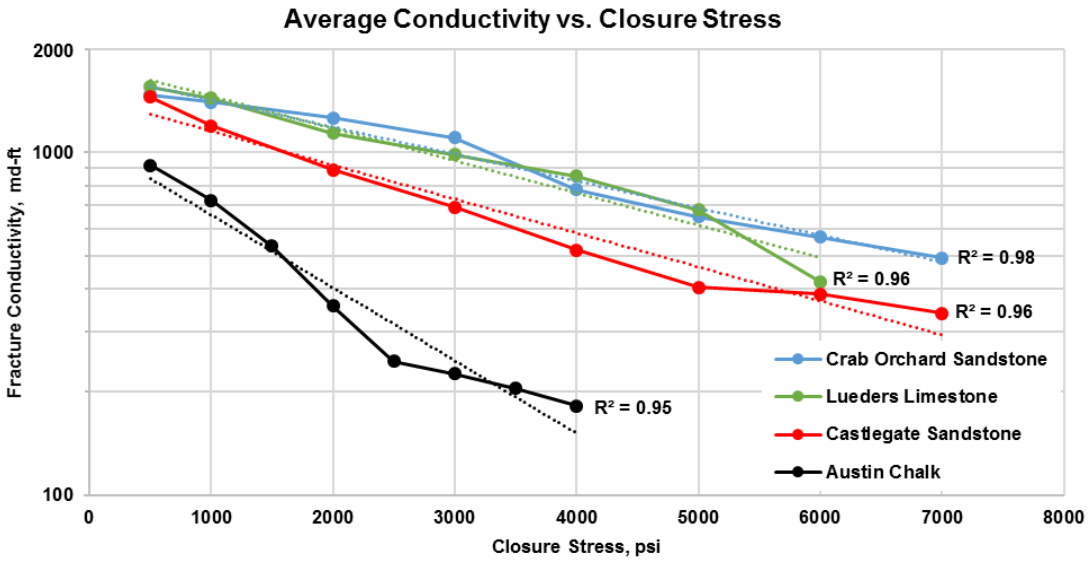

Figure 31-Average conductivity values at each closure stress for the four different rock types.

Initial average conductivity values at 500 psi closure stress were essentially the same for the Crab Orchard, Lueders, and Castlegate samples. This was expected due to the same proppant loading conditions and very little proppant embedment taking place at a lower closure stress. However, the Austin chalk samples already showed signs of initial fracture width reduction at 500 psi and experienced the steepest decline of conductivity as closure stress was gradually increased. Crab Orchard and Lueders samples experienced similar conductivity behaviors with the shallowest declines. The change in displacement of the hydraulic piston from its initial position as closure stress is increased confirms the behavior seen in the conductivity curves. **Figure 32** shows the average change in piston displacement for each of the four rock types during conductivity testing.

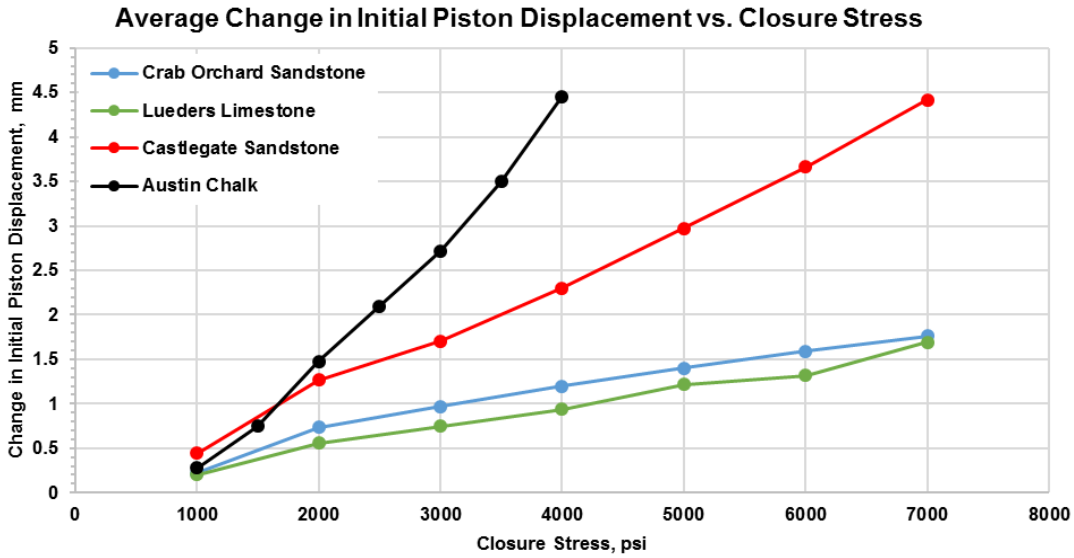

Figure 32-Average change in piston displacement showing the steepest change of movement in the Austin chalk samples.

The Austin chalk samples showed the most dramatic change of approximately 4.5 mm at 4,000 psi closure stress, followed by the Castlegate sandstone samples. Lueders and Crab Orchard showed the least amount of displacement and followed similar trends with each other. These curves were generated by monitoring the position of the hydraulic piston used to apply vertical stress to the fracture, at a precision of 0.0001 mm. Included in this displacement value is axial contraction of the rock matrix, compaction of the proppant pack, and embedment of the proppant grains into the fracture face. Therefore, these displacement curves cannot be directly attributed to a reduction in fracture width, but still give valuable insight helping to explain differences in conductivity behavior. Displacement curves would be useful in comparing before and after the fracture has been exposed to a liquid, as differences between the two would be directly related to increased proppant embedment from surface interactions with the liquid.

4.2 Brinell Hardness Results

Average values of Brinell hardness from six tests on each rock type are shown in Table 3. For each sample, two different ratios of applied force to the diameter of the indenter were used to ensure accuracy of the measurements.

Table 3-Average Brinell hardness values for each rock type.

Formation	Average HBW, kgf/mm^2	Indentation depth at .5 kN, mm
Crab Orchard Sandstone	272.72	0.02
Lueders Limestone	47.41	0.11
Castlegate Sandstone	13.83	0.37
Austin Chalk	8.40	0.61

Hardness values across the four rock types had a wide range from 8 to 275 kgf/mm^2, with Crab Orchard as the hardest surface followed by Lueders, Castlegate, and Austin chalk as the softest. Indentation depths are also shown for the .5 kN tests, calculated using **Eq. 19** below,

$$h = \frac{D-\sqrt{D^2-d^2}}{2} \quad \text{.....(19)}$$

where D is the diameter of the indenter ball in mm, and d is the measured mean diameter of the indentation in mm.

4.3 Triaxial Test Results

Triaxial compressive tests were performed on at least two cylindrical one inch diameter by two inches tall core plugs from each rock type. A 2-Mpa (≈290 psi) confining pressure was applied to each sample during testing to aid in maintaining sample integrity. Multiple loading cycles were used to remove any inelastic behavior from the rock matrix

before determining the elastic moduli. Once sufficient stress-strain curves were obtained, it was attempted to make the sample undergo compressive failure and obtain the strength of the rock. All raw stress-strain data for each sample along with interpretations of the curves can be found in the Appendix. **Figures 33-35** show the results for average Young's modulus, Poisson's ratio, and compressive strength respectively across the four different rock types, with error bars representing the standard deviation between multiple measurements.

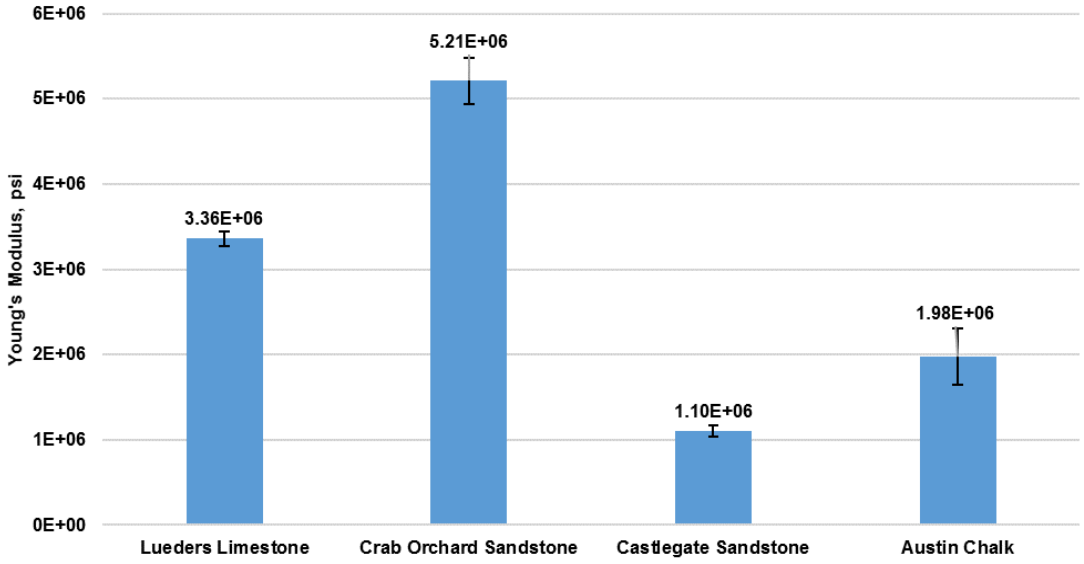

Figure 33-Young's modulus average results with standard deviations.

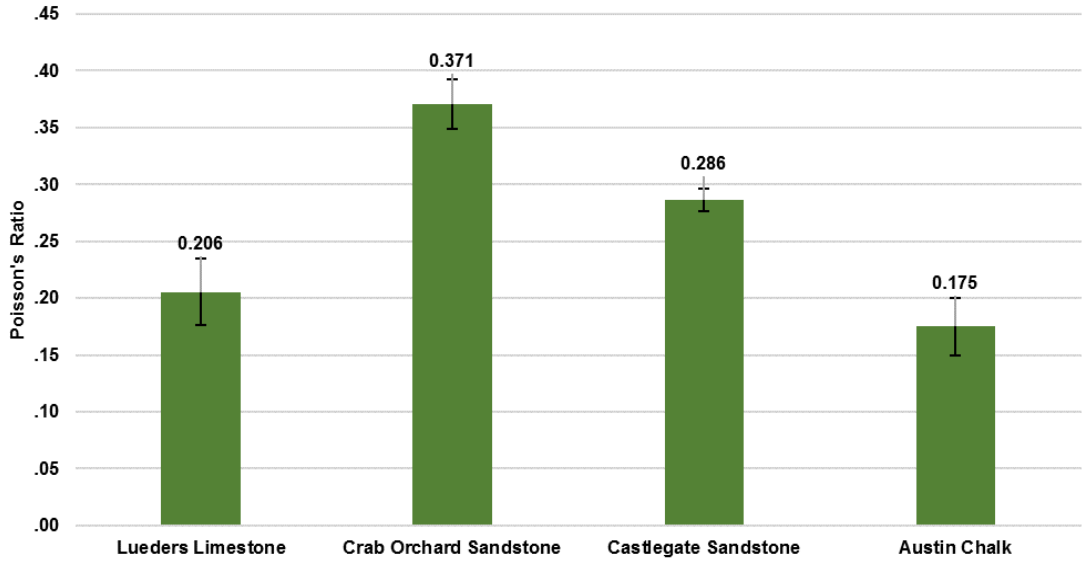

Figure 34-Poisson's ratio average results with standard deviations.

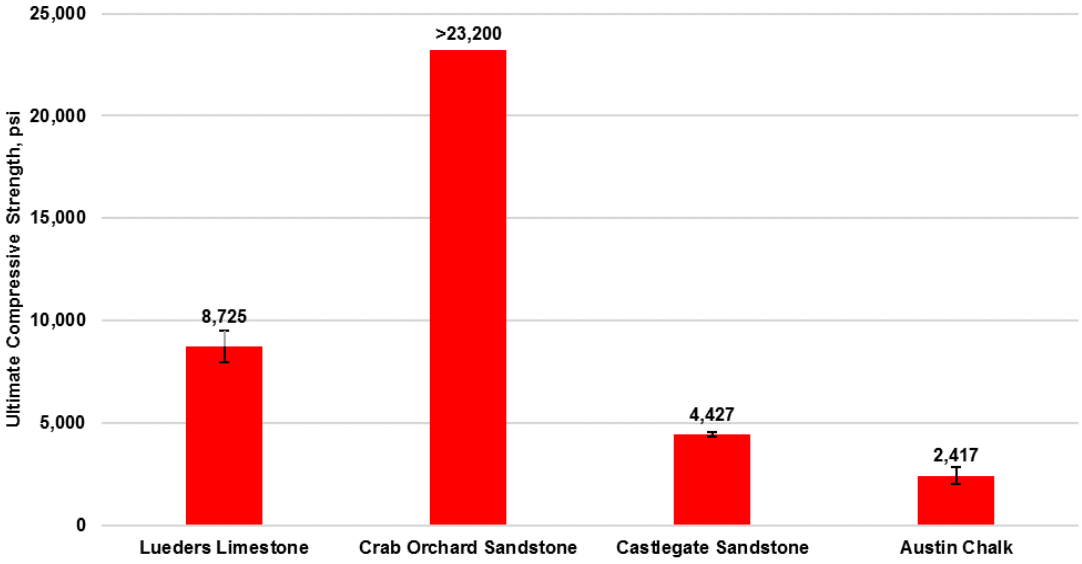

Figure 35-Compressive strength average results with standard deviations

Once again, a broad range in properties were obtained across the four different rock types. Variability between individual tests was low due to using all homogeneous rocks and carefulness taken during sample preparation. It is important to note that the Crab Orchard samples were never brought to the point of compressive failure due to fear of damaging the testing equipment. However, the highest stress experienced by these samples while remaining intact was 23,200 psi. The mechanical properties results for individual samples are summarized in the Appendix.

4.4 Effects of Rock Mechanical Properties on Fracture Conductivity

This section discusses each individual mechanical property's role in affecting fracture conductivity based on these experimental results and previous works. Validation for how each are incorporated into the correlation models is also provided.

4.4.1 Young's Modulus

Young's modulus, commonly referred to as the elastic modulus, is a measure of how stiff a material behaves. It is the ratio between the amount of axial stress applied and the resulting strain/deformation the material experiences in the axial direction. This parameter only explains the stress-strain relationship during elastic behavior of the material. For a rock to behave elastically, it must return to its original shape and position once the applied axial stress is removed. As stresses increase, the rock may undergo inelastic/plastic deformation in which case Young's modulus is no longer meaningful. Alramahi and Sundberg (2012) studied the relationship between Young's modulus and the

degree of proppant embedment in shales, and were able to derive the power law relationship shown in **Figure 36**.

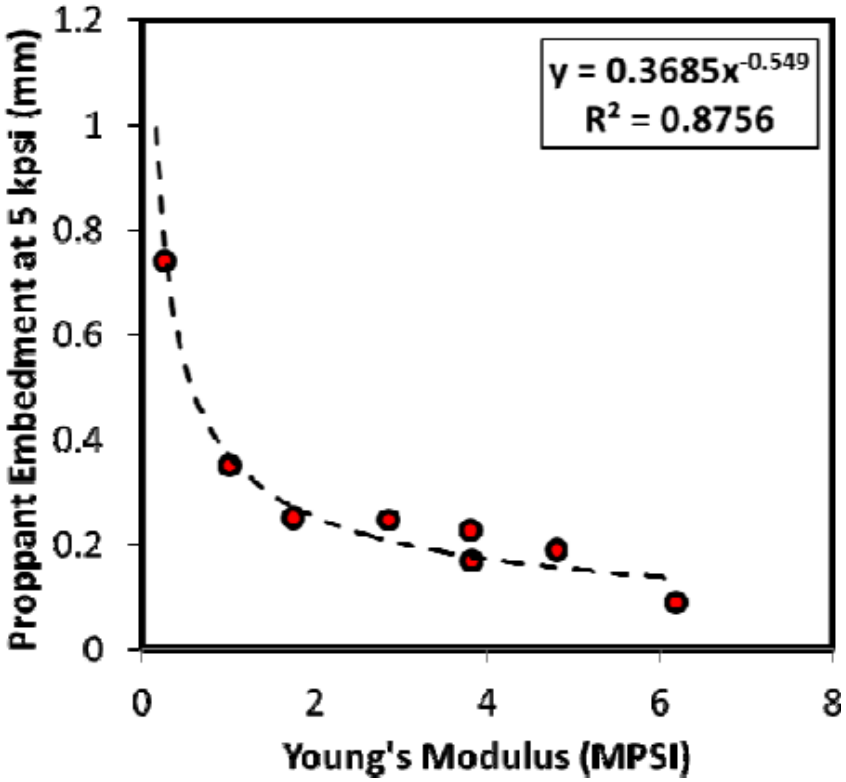

Figure 36-Power law relationship between proppant embedment and static Young's modulus at 5,000 psi closure stress (reprinted from Alramahi and Sundberg 2012).

However, these results are counter intuitive as proppant embedment is a result of inelastic deformation at the fracture face, at which point Young's modulus no longer applies (Perez-Pena 2015). Embedment should be more closely associated with the yield point or compressive strength of the rock matrix, both of which are properties associated with the inelastic portion of the stress-strain curve. This power law relationship is likely the result of collinearity between Young's modulus and another mechanical property, none of which

were reported in the paper. The authors were also able to relate their embedment tests to fracture conductivity experiments. Rocks with severe proppant embedment (low modulus) experienced steep declines and high losses of conductivity with increased closure stress. **Figure 37** compares the average exponential decline rate from the conductivity experiments with average values of Young's modulus.

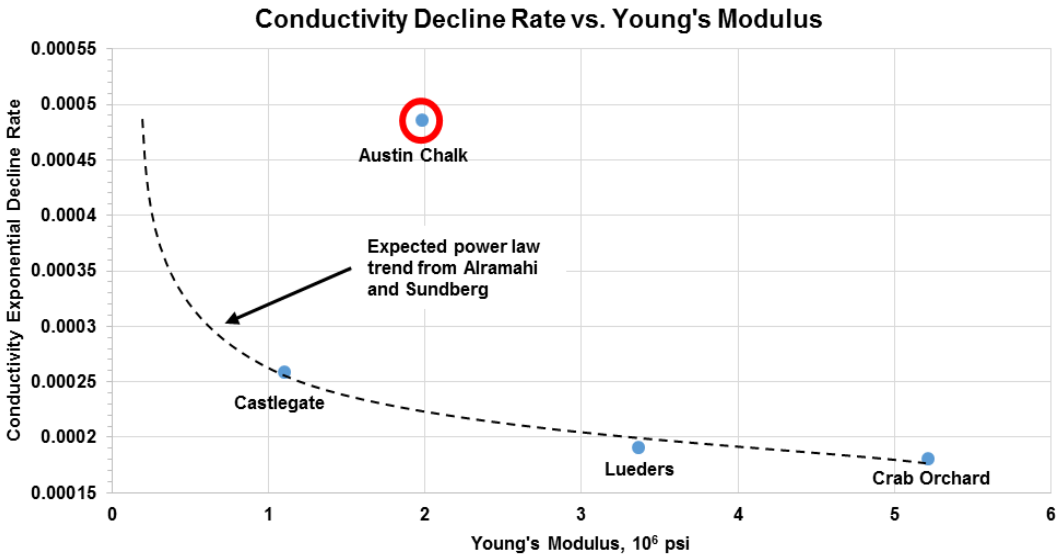

Figure 37-Conductivity decline rate vs. Young's modulus with Austin Chalk as outlier.

The Austin chalk is an important outlier in this plot, which had nearly twice the rate in conductivity decline as the Castlegate sandstone, but also approximately double the value of static Young's modulus. Therefore, confirming the false relationship between elastic modulus and conductivity decline due to proppant embedment. In order to properly understand the effect of Young's modulus, we must first be able to visualize what is

occurring inside the fracture as closure stress is increased. **Figure 38** represents a typical induced fracture with surface asperities and a low proppant concentration.

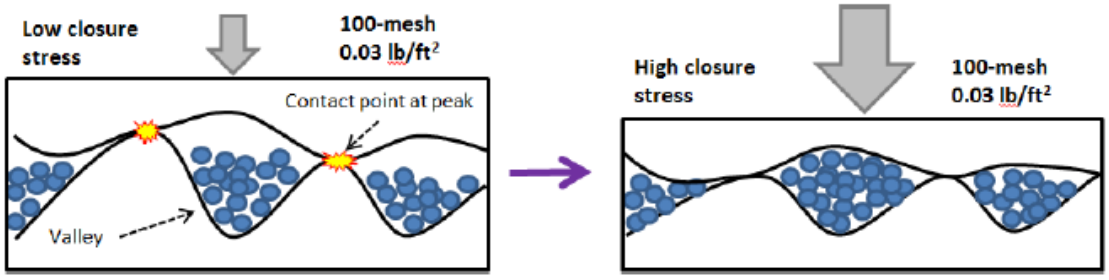

Figure 38-Typical proppant distribution at low proppant concentrations in an induced fracture (reprinted from Kamenov 2013).

Due to the presence of surface asperities and a low number of proppant layers, there exists regions inside the fracture of rock-rock interactions. In these areas, fracture aperture reduction is due to an axial strain of the rock matrix, which could best be explained/quantified by the elastic modulus of the rock. The magnitude and presence of this effect is highly dependent on the number of proppant layers, and hence the proppant concentration inside the fracture. At high concentrations, rock-rock interactions between the fracture faces may be non-existent and the dominant cause of aperture reduction with respect to the rock properties becomes proppant embedment. Because the magnitude of the effect of Young's modulus is dependent on proppant concentration, the presence of an interaction term between these two parameters should be investigated in the predictive models for conductivity.

4.4.2 Brinell Hardness

As stated earlier, Brinell hardness is a surface indentation test quantifying how resistive the rock's surface is to embedment of a spherical indenter. Since Brinell hardness is being used to help explain fracture conductivity reduction due to proppant embedment, it is important to understand the relationship between the Brinell hardness number and the actual depth of the indentation. **Figure 39** shows the indentation depth of the 1/8" spherical indenter used in the test under 0.5 kN of applied force versus the actual Brinell hardness number. These calculations were made using Eqs. 7 and 13 presented previously and neither values were directly measured.

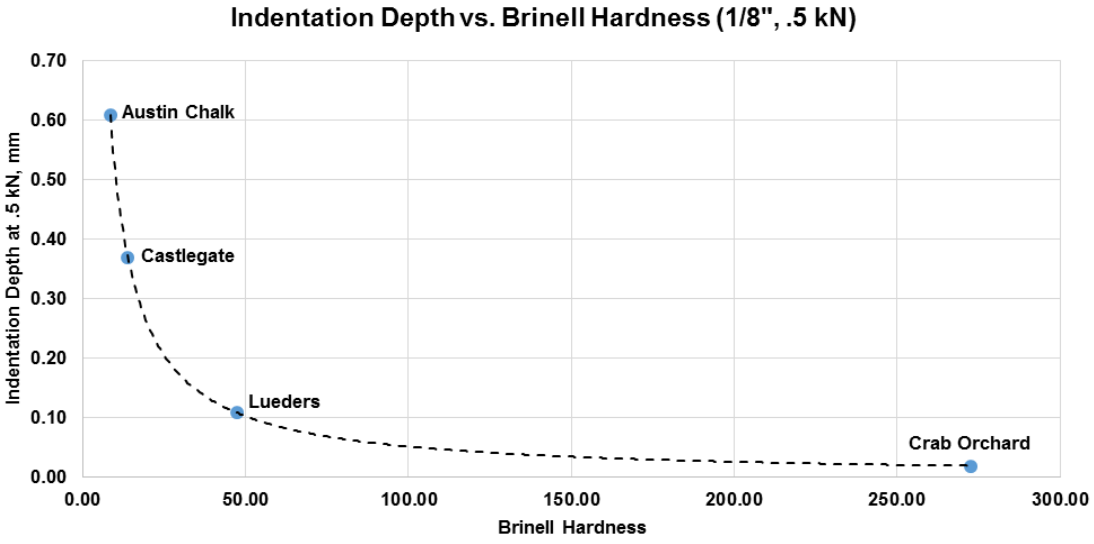

Figure 39-Indentations Depth vs. Brinell Hardness displaying the inherent power law relationship.

Due to the inherent relationship between indentation depth and Brinell hardness, a perfect power law relationship exists between these two values. Obviously, indentation depth varies for the same Brinell hardness value based on indenter size and applied force, however, the power law relationship always holds true. This is important to clarify as it determines the expected response in conductivity behavior and how the Brinell hardness parameter should be treated in any statistical model. **Figure 40** displays the relationship between Brinell hardness and the rate of decline in conductivity from this study.

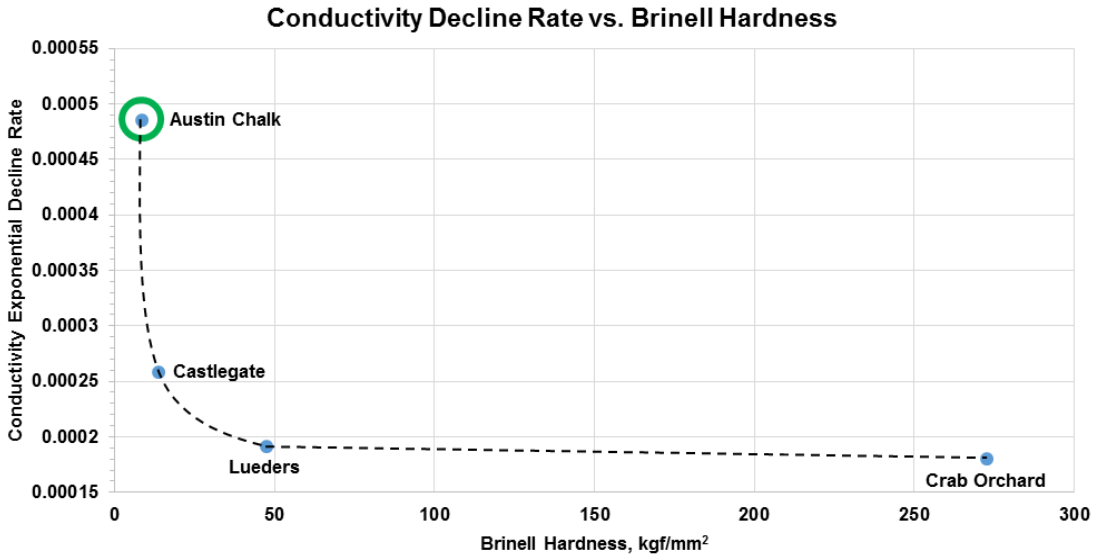

Figure 40-Conductivity decline rate vs. Brinell hardness showing a much better relationship than Young's modulus, with Austin chalk no longer an outlier.

Analogous to Figure 37, which compares the elastic modulus, Figure 40 shows an improved relationship between Brinell hardness and conductivity decline. This is expected due to Brinell hardness better quantifying plastic deformation at the fracture surface and its underlying power law relation with indentation depth. Therefore, the

natural log transformation should be applied to both fracture conductivity and Brinell hardness to linearize their relationship in the regression model.

4.4.3 Compressive Strength

Compressive strength is the point at which a rock undergoes either ductile or brittle failure under increasing compressive stresses. Compressive strength in this study was taken at the point where the slope of the stress-strain curve was approximately zero. As mentioned previously, this parameter is associated with inelastic deformation of a material as opposed to Young's modulus, which is concerned with the elastic behavior region. Compressive strength can vary significantly with the amount of confining pressure a material is experiencing. 2-MPa confining pressure on the samples was used throughout the triaxial tests. **Figure 41** shows the relationship between compressive strength and the exponential decline rate of the fracture conductivity. As a reminder, the Crab Orchard samples were not taken all the way to failure and the value displayed here is the highest stress the samples underwent.

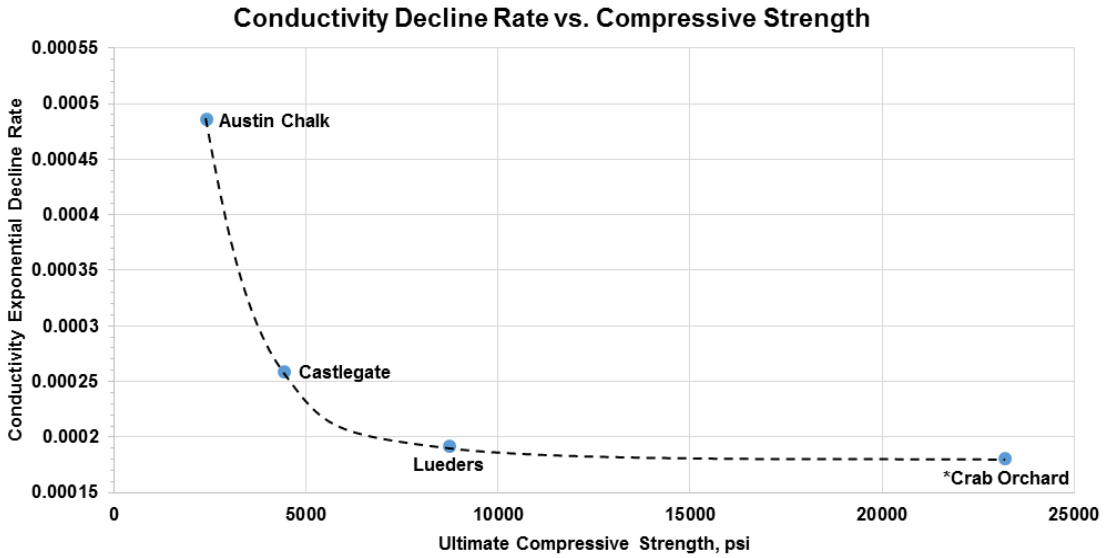

Figure 41-Conductivity decline rate vs. Compressive strength of the rock matrix.

Once again, a power law relationship exists with compressive strength explaining the rate of decline in conductivity. Similar trends with both Brinell hardness and compressive strength is a strong indication that these two parameters could be linearly related. **Figure 42** displays the relationship between Brinell hardness and compressive strength.

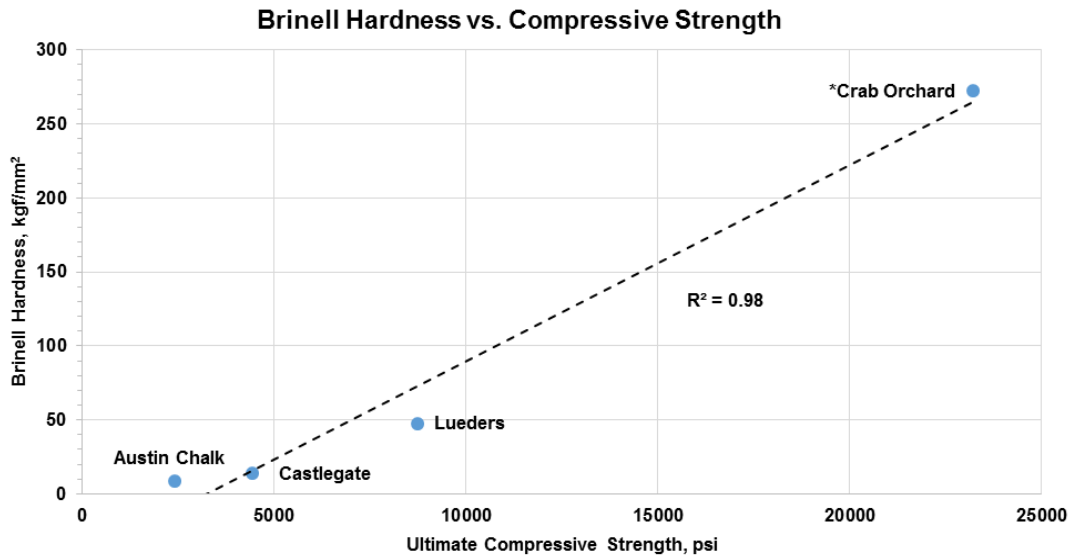

Figure 42-Displays linearity between Brinell hardness and Compressive strength.

As can be seen in Figure 42, a strong linear relationship exists between these two variables. Therefore, both of these parameters have the ability to explain the same behavior in fracture conductivity and only one should be included in the regression model to avoid collinearity between predictors. Brinell hardness is given priority since it focuses on the behavior at the fracture face itself, as opposed to the entire matrix of the rock. Brinell hardness should be more sensitive to proppant embedment as well as any fluid effects occurring on the fracture surface. Compressive strength is still valuable in instances where Brinell hardness is highly uncertain and because of its ability to be estimated from downhole sonic logs.

4.4.4 Poisson's Ratio

Poisson's ratio quantifies a materials tendency to elastically deform perpendicularly to an applied axial stress. It is calculated as the ratio of axial strain to lateral strain. In the field, Poisson's ratio is important as it determines the magnitude of closure stress on a vertical fracture transferred from the overburden stress. **Figure 43** represents a typical underground stress state where the overburden stress from overlying rock layers is the maximum principal stress.

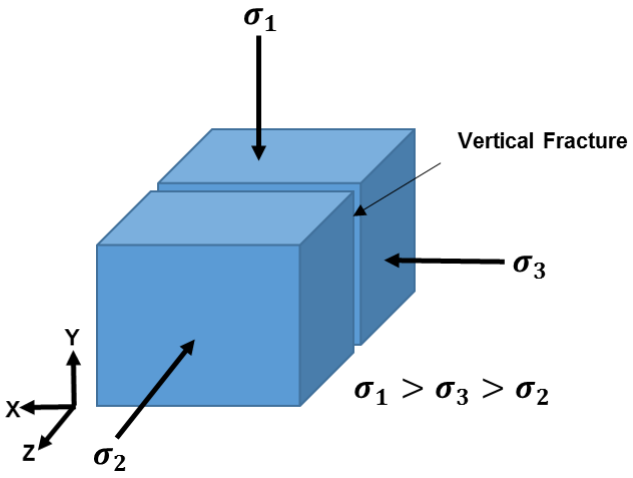

Figure 43-Typical in the field stress state resulting in a vertical fracture.

Fractures open in the direction of and propagate perpendicular to the minimum principal stress. In this case of a vertical fracture and the assumption of plane strain, the minimum horizontal/closure stress can be estimated with **Eq. 20,**

$$\sigma_2 = \sigma_{min} \cong \frac{\nu}{1-\nu}\left(\sigma_1 - \alpha p_p\right) + \alpha p_p + \sigma_{ext} \quad \text{.....(20)}$$

where σ_{min} is the minimum horizontal stress, ν is Poisson's ratio, σ_1 is overburden stress, α is Biot's constant, p_p is pore pressure inside the fracture, and σ_{ext} are any tectonic stresses present. The main takeaway from this equation is that Poisson's ratio is used to transform the vertical overburden stress into an effective horizontal stress acting on the fracture. However, during the conductivity experiments, principal stresses and their magnitudes relative to the fracture are as shown in **Figure 44**.

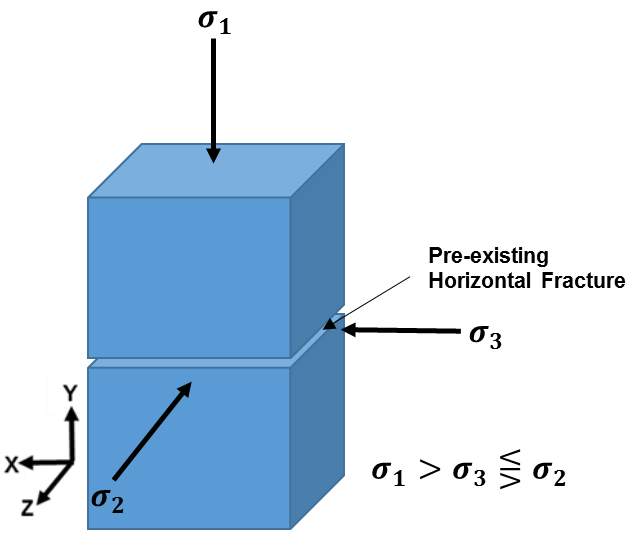

Figure 44-Experimental stress state for a pre-existing horizontal fracture.

In the experimental case, a horizontal fracture is already present before any stresses are applied. σ_1, the closure and max principal stress on the fracture, is manually controlled by the hydraulic piston applying a distributed force to the sample. Because the sample is confined in all directions by the conductivity cell, plane strain could be assumed and the horizontal stresses become a function of σ_1 and Poisson's ratio, as in Eq. 20. However, the assumption of plane strain may not be entirely valid as the epoxy surrounding the

sample can deform into any void spaces where the flow inlet/outlet and pressure ports exist. Nonetheless, using the principle behind Eq. 20 and assuming plane strain, an induced horizontal stress on the sample from the vertical force applied by the piston can be estimated. Results are shown in **Figure 45** for a range of Poisson's ratios at a closure stress of 5,000 psi.

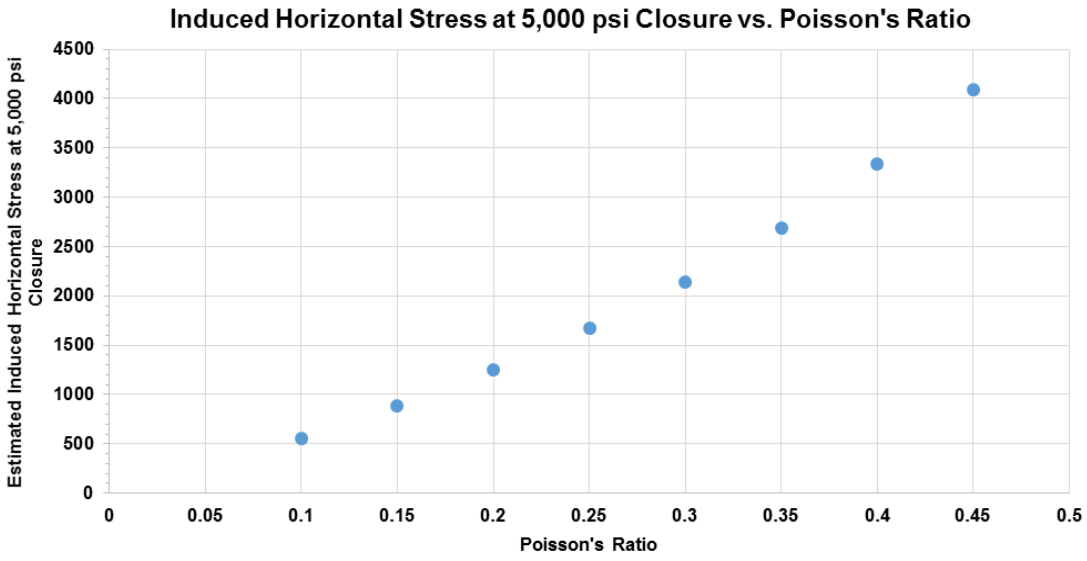

Figure 45-Estimated horizontal stresses experienced by the sample with respect to a range of Poisson's ratio at 5,000 psi closure stress.

It is well known that rock mechanical properties can change drastically based on the amount of horizontal confining pressure the rock is experiencing (Blanton 1981). Due to the large range and relatively high values of induced horizontal stress inside the experimental setup, Poisson's ratio could be playing a significant role by altering the mechanical properties at the fracture face. However, no meaningful correlations between fracture conductivity and Poisson's ratio were found in this study.

5. CONCLUSIONS AND RECOMMENDATIONS

5.1 Conclusions

This work presents the generation of a shale fracture conductivity correlation based on a large database of experimental data from previous researchers at Texas A&M University. A comprehensive study of the effects that different mechanical rock properties have on fracture conductivity was performed. Previous experimental variables were eliminated and the properties of Young's modulus, Poisson's ratio, compressive strength, and Brinell hardness were isolated during conductivity testing. The resulting relationships between these parameters were analyzed to improve prediction of conductivity and future characterization of rock mechanical properties. The main conclusions of this work are summarized below:

(1) Brinell hardness and compressive strength are highly correlated with fracture conductivity decline caused by inelastic deformation of the fracture face, resulting in proppant embedment and consequently a reduction in aperture.

(2) Closure stress and proppant loading conditions have a much greater influence on fracture conductivity when compared to rock mechanical properties and fracture surface characteristics.

(3) Young's modulus is a highly significant predictor of fracture conductivity in shales. A higher modulus correlated to increased conductivity at each closure stress.

(4) Brinell hardness was found to have a power law relationship with fracture conductivity decline in the rock properties study, as well as a direct correlation with conductivity in the Eagle Ford data set.

(5) The final correlation model presented can be used to estimate fracture conductivity in various shale plays. It is important to keep in mind the distributions of the input data into the model, as well as the experimental conditions under which the conductivity was measured when applying this correlation for prediction purposes.

5.2 Recommendations and Limitations

This work can be improved upon and expanded in many ways. The following contains limitations to this study and recommendations for future work in this area:

(1) Brinell hardness and compressive strength should be standard mechanical properties measured on conductivity samples to better explain trends in conductivity decline.

(2) A correction for water damage should be added to the conductivity correlation. This could be accomplished by combining previous and future conductivity experiments on shales tailored towards quantifying the recovery of conductivity after water exposure and relating this quantity to mineralogy of the rock or other properties.

(3) Brinell hardness could be measured with and without exposure to water in order to quantify the effect of water damage on many different shales, as opposed to running full conductivity tests with water.

(4) Gaps in the historical shale conductivity data such as Brinell hardness and compressive strength could be filled to better refine the correlation and make it applicable to a broader range of conditions.

(5) Empirical correlations are just the first step in attempting to model these processes physically and should provide an insightful foundation for future theoretical work in this area.

REFERENCES

API RP 61, Recommended Practice for Evaluating Short-Term Proppant-Pack Conductivity. 1989. Washington, DC: API.

Akrad,O., Miskimins, J., Prasad, M. 2011. The effects of Fracturing Fluids on Shale Rock Mechanical Properties and Proppant Embedment. SPE Annual Technical Conference and Exhibition. Denver, CO. 2011. SPE-146658-MS. DOI: 10.2118/146658-MS.

Alramahi, B., Sundberg, M.I. 2012. Proppant Embedment and Conductivity of Hydraulic Fractures in Shales. US Rock Mechanics / Geomechanics Symposium. Chicago, Illinois. 2012. Copyright 2012 ARMA, American Rock Mechanics Association.

ASTM Standard D7012-14. Standard Test Methods for Compressive Strength and Elastic Moduli of Intact Rock Core Specimens under Varying States of Stress and Temperatures. 2014. West Conshohocken, PA: ASTM International. DOI: 10.1520/D7012-14.

ASTM Standard E10-14. Standard Test Method for Brinell Hardness of Metallic Materials. 2015. West Conshohocken, PA: ASTM International. DOI: 10.1520/E0010-15A.

Barton, N. R., Bandis, S. C., Bakhtar, K. 1985. Strength, deformation and conductivity coupling of rock joints. *International Journal of Rock Mechanics and Mining Sciences & Geomechanics*.

Barree, R. D., S. A. Cox, V. L. Barree et al. 2003. Realistic Assessment of Proppant Pack Conductivity for Material Selection. SPE Annual Technical Conference and Exhibition, Denver, CO. 2011. SPE-84306-MS. DOI: 10.2118/84306-MS.

Barree, R.D., Miskimins, J.L., Conway, M.W. et al. 2016. Generic Correlations for Proppant Pack Conductivity. Hydraulic Fracturing Technology Conference, The Woodlands, TX. 2016. SPE-179135-MS. DOI: 10.2118/179135-MS.

Blanton, T.L. 1981. Deformation of Chalk under Confining Pressure and Pore Pressure. *Society of Petroleum Engineers Journal.* SPE-8076-PA. DOI: 10.2118/8076-PA.

Briggs, K. E. 2014. The Influence of Vertical Location on Hydraulic Fracture Conductivity in the Fayetteville Shale. M.S. Thesis, Texas A&M University, College Station, Texas (May 2014).

Cooke Jr. C.E 1973. Conductivity of Fracture Proppants in Multiple Layers. *Journal of Petroleum Technology*. SPE-4117-PA. DOI: 10.2118/4117-PA.

Cooke Jr. C.E 1975. Effect of Fracturing Fluids on fracture Conductivity. *Journal of Petroleum Technology*. SPE-5114-PA. DOI: 10.2118/5114-PA.

Das, P., Achalpurkar, M. 2013. Impact of Rock Mechanics and Formation Softening Analysis in Shale Fracturing Design. SPE Kuwait Oil and Gas Show and Conference, Mishref, Kuwait 2013. SPE-167336-MS. DOI: 10.2118/167336-MS.

Enriquez Tenorio, O. 2016. A comprehensive study of the Eagle Ford shale fracture conductivity. M.S. Thesis, Texas A&M University, College Station, Texas (May 2016).

Fredd, C.N., McConnell, S.B., Boney, C.L. et al. 2001. Experimental Study of Fracture Conductivity for Water-Fracturing and Conventional Fracturing Applications. *SPE Journal.* SPE-74138-PA. DOI: 10.2118/74138-PA.

Guerra, J., Zhu D., Hill, A.D. 2017. Impairment of Fracture Conductivity in the Eagle Ford Shale Formation. SPE Hydraulic Fracturing Technology Conference and Exhibition, The Woodlands, TX. 2017. SPE-184857-MS. DOI: 10.2118/184857-MS.

Huitt, J.L. and McGlothlin, B.B. 1958. The propping of fractures in formations susceptible to propping sand embedment. Drilling and Production Practice. American Petroleum Institute.

ISO 13503-5:2006, International Organization for Standardization: Procedures for measuring the long-term conductivity of proppants. 2006. Geneva, Switzerland: ISO.

Jansen, T.A., 2014. The Effect of Rock Properties on Hydraulic Fracture Conductivity in the Eagle Ford and Fayetteville Shales. MS thesis, Texas A&M University, College Station, Texas (December 2014).

Kamenov, A.N 2013. The Effect of Proppant Size and Concentration on Hydraulic Fracture Conductivity in Shale Reservoirs. MS thesis, Texas A&M University, College Station, Texas (May 2013).

Knorr, A, F. 2016. The Effect of Mechanical Properties on Fracture Conductivity in the Eagle Ford. M.S. Thesis, Texas A&M University, College Station, Texas (May 2016).

Makurat, A. and Gutierrez, M. 1996. Fracture Flow and Fracture Cross Flow Experiments. Society of Petroleum Engineers. SPE Annual Technical Conference and Exhibition, Denver, CO. 1996. SPE-36732-MS. DOI: 10.2118/36732-MS.

McGinley, M.J 2015. The Effect of Fracture Orientation and Anisotropy on Hydraulic Fracture Conductivity in the Marcellus Shale. MS thesis, Texas A&M University, College Station, Texas (May 2015).

Mueller, M., Amro, M. 2015. Indentation Hardness for Improved Proppant Embedment Prediction in Shale Formations. SPE European Damage Conference and Exhibition, Budapest, Hungary. 2015. SPE-174227-MS. DOI: 10.2118/174227-MS.

Palisch, T., Duenckel, R., Bazan, L., Heidt, H.J., and Turk, G. 2007. Determining Realistic Fracture Conductivity and Understanding its Impact on Well Performance-Theory and Field Examples. SPE Hydraulic Fracturing Technology conference, College Station, TX. 2007. SPE-106301-MS. DOI: 10.2118/106301-MS.

Parker, M., Glasbergen, G., van Batenburg, D.W., Weaver, J.D., and Slabaugh, B.F. 2005. High-Porosity Fractures Yield High Conductivity. SPE Annual Technical Conference and Exhibition, Dallas, TX. 2005. SPE-96848-MS. DOI: 10.2118/96848-MS.

Perez Pena, P.A. 2015. The Effect of Rock Properties on Fracture Conductivity in the Marcellus Shale. MS thesis, Texas A&M University, College Station, Texas (May 2015).

Ramurthy, M., Barree, R.D., Kundert, D.P., Petre, E., and Mullen, M. 2011. Surface-Area vs Conductivity-Type Fracture Treatments in Shale Reservoirs. *SPE Production and Operations*. SPE-140169-PA. DOI: 10.2118/140169-PA.

Tek, M.R., Coats, K.H., and Katz, D.L. 1962. The Effect of Turbulence on Flow of Natural Gas through Porous Reservoirs. *SPE Journal*. SPE-147-PA. DOI: 10.2118/147-PA.

Terracina, J.M., Turner, J.M., Collins, D.H., and Sillars, S.E. 2010. Proppant selection and its effect on the results of fracturing treatments performed in shale formations. SPE Annual Technical Conference and Exhibition, Florence, Italy. 2010. SPE-135502-MS. DOI:10.2118/135502-MS.

Zhang, J., Lianchen O., Hill, A.D. et al. 2014. Experimental and Numerical Studies of Reduced Fracture Conductivity due to Proppant Embedment in Shale Reservoirs. SPE Annual Technical Conference and Exhibition, Amsterdam, The Netherlands. 2014. SPE-170775-MS. DOI: 10.2118/170775-MS.

Zhang, J.. 2014. Creation and Impairment of Hydraulic Fracture Conductivity in Shale Formations. Ph.D. Dissertation, Texas A&M University, College Station, Texas (May 2014).

Zhang, J., Kamenov, A., Hill, A.D. et al. 2014. Laboratory Measurement of Hydraulic-Fracture Conductivities in the Barnett Shale. *SPE Production & Operations*. SPE-163839-PA. DOI: 10.2118/163839-PA.

APPENDIX

	Lueders Limestone		
	Young's Modulus, psi	Poisson's Ratio	Ultimate Compressive Strength, psi
Sample 1	3.42E+06	0.185	8190
Sample 2	3.30E+06	0.226	9260
Sample 3	-	-	-
Average	3.36E+06	0.206	8725
Standard Deviation	8.53E+04	0.029	757
Percent Standard Deviation	2.54%	14.27%	8.67%

	Crab Orchard Sandstone		
	Young's Modulus, psi	Poisson's Ratio	*Ultimate Compressive Strength, psi
Sample 1	4.91E+06	0.348	>15500
Sample 2	5.28E+06	0.374	>18850
Sample 3	5.44E+06	0.390	>23200
Average	5.21E+06	0.371	-
Standard Deviation	2.68E+05	0.021	-
Percent Standard Deviation	5.15%	5.78%	-

*Samples never brought to failure

	Castlegate Sandstone		
	Young's Modulus, psi	Poisson's Ratio	Ultimate Compressive Strength, psi
Sample 1	1.15E+06	0.293	4495
Sample 2	1.06E+06	0.279	4358
Sample 3	-	-	-
Average	1.10E+06	0.286	4427
Standard Deviation	6.26E+04	0.010	97
Percent Standard Deviation	5.67%	3.40%	2.19%

	Austin Chalk		
	Young's Modulus, psi	Poisson's Ratio	Ultimate Compressive Strength, psi
Sample 1	1.74E+06	0.157	2703
Sample 2	2.21E+06	0.193	2130
Sample 3	-	-	-
Average	1.98E+06	0.175	2417
Standard Deviation	3.31E+05	0.025	405
Percent Standard Deviation	16.74%	14.52%	16.77%

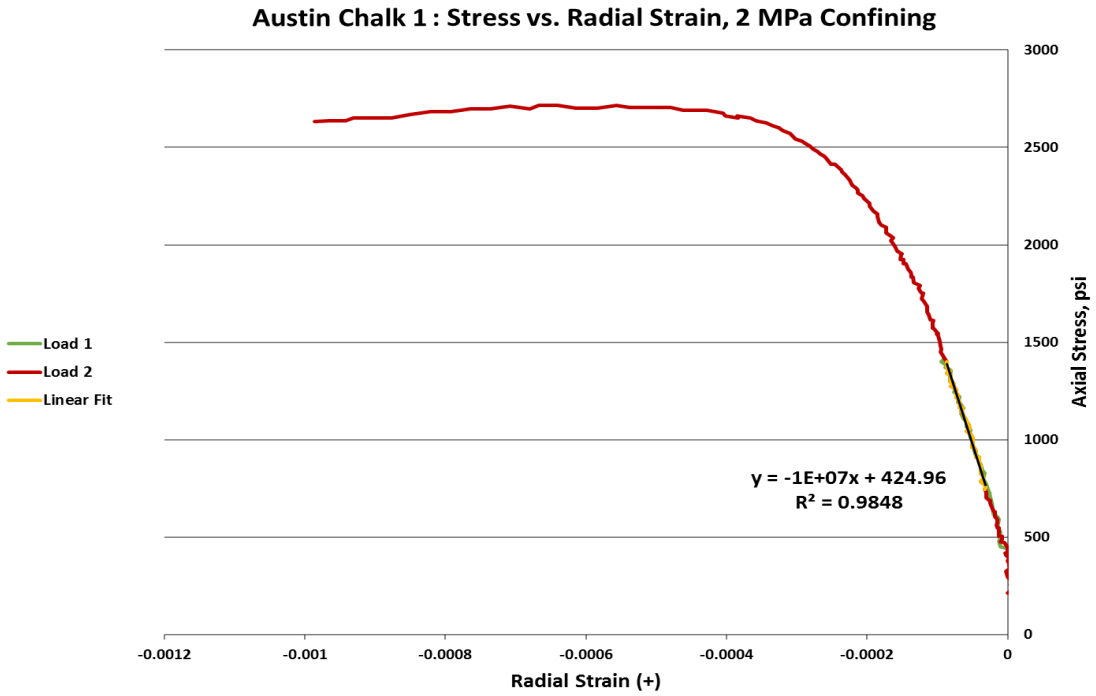

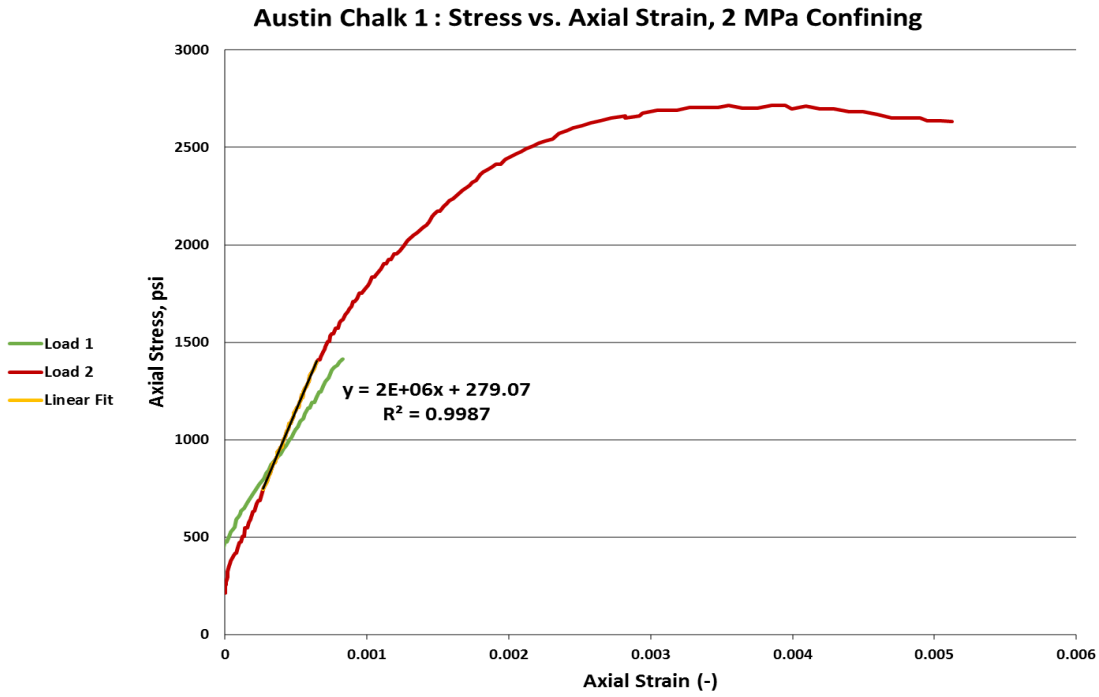
Austin Chalk 1 : Stress vs. Axial Strain, 2 MPa Confining
Load 1
Load 2
Linear Fit
y = 2E+06x + 279.07
R² = 0.9987
Axial Stress, psi
Axial Strain (-)
3000
2500
2000
1500
1000
500
0
0
0.001
0.002
0.003
0.004
0.005
0.006

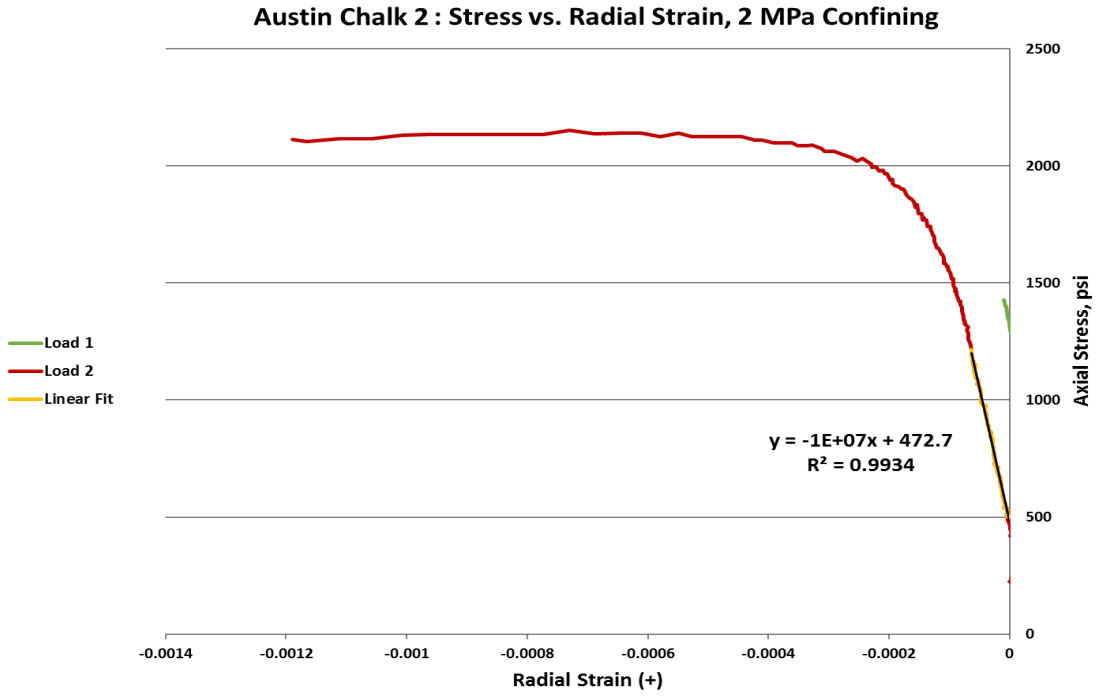
Austin Chalk 2 : Stress vs. Radial Strain, 2 MPa Confining
Load 1
Load 2
Linear Fit
y = -1E+07x + 472.7
R² = 0.9934
Axial Stress, psi
Radial Strain (+)
2500
2000
1500
1000
500
0
-0.0014
-0.0012
-0.001
-0.0008
-0.0006
-0.0004
-0.0002
0

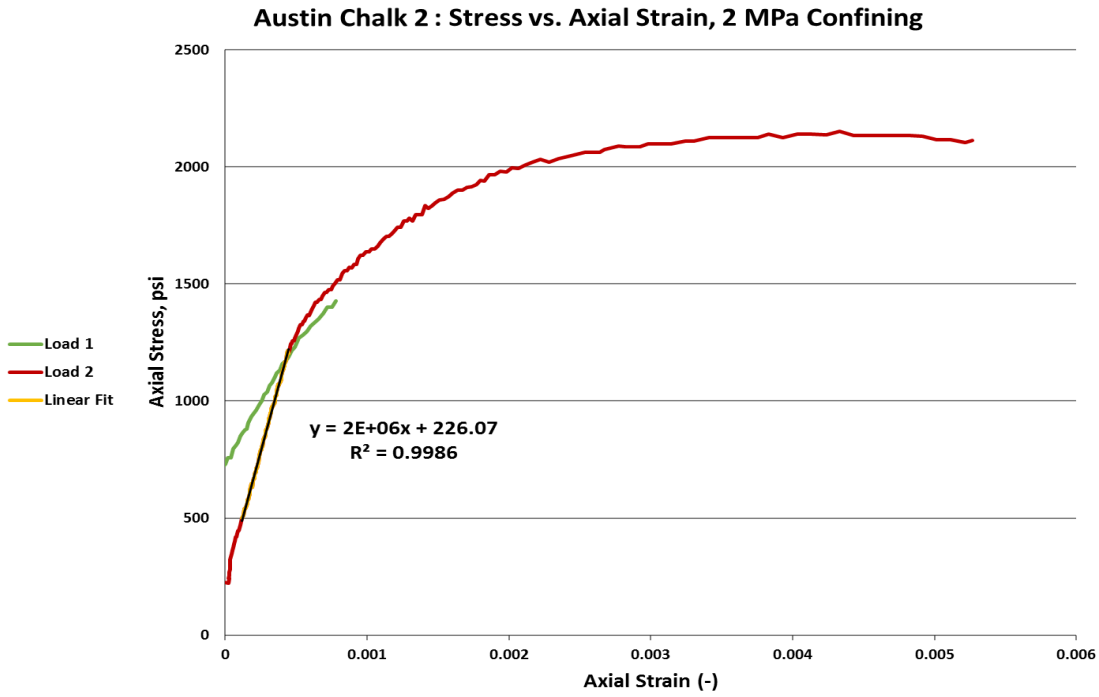
Austin Chalk 2 : Stress vs. Axial Strain, 2 MPa Confining
Load 1
Load 2
Linear Fit
Axial Stress, psi
2500
2000
1500
1000
500
0
y = 2E+06x + 226.07
R² = 0.9986
0
0.001
0.002
0.003
0.004
0.005
0.006
Axial Strain (-)

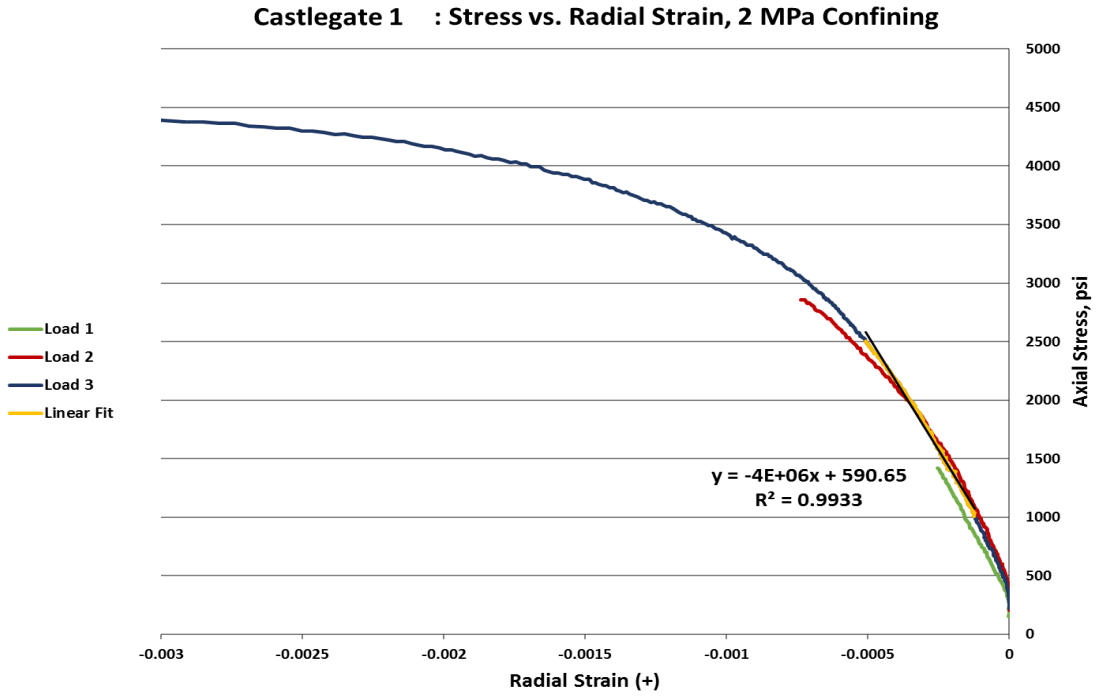
Castlegate 1 : Stress vs. Radial Strain, 2 MPa Confining
Load 1
Load 2
Load 3
Linear Fit
Axial Stress, psi
5000
4500
4000
3500
3000
2500
2000
1500
1000
500
0
y = -4E+06x + 590.65
R² = 0.9933
-0.003
-0.0025
-0.002
-0.0015
-0.001
-0.0005
0
Radial Strain (+)

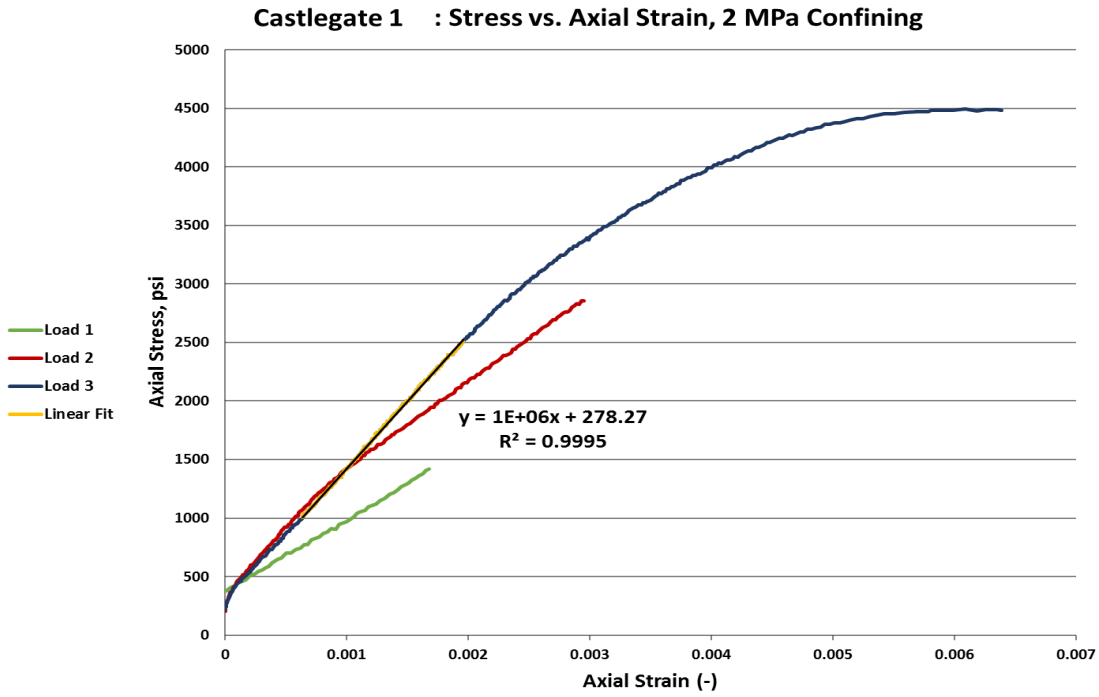
Castlegate 1 : Stress vs. Axial Strain, 2 MPa Confining
Load 1
Load 2
Load 3
Linear Fit
Axial Stress, psi
5000
4500
4000
3500
3000
2500
2000
1500
1000
500
0
y = 1E+06x + 278.27
R² = 0.9995
0
0.001
0.002
0.003
0.004
0.005
0.006
0.007
Axial Strain (-)

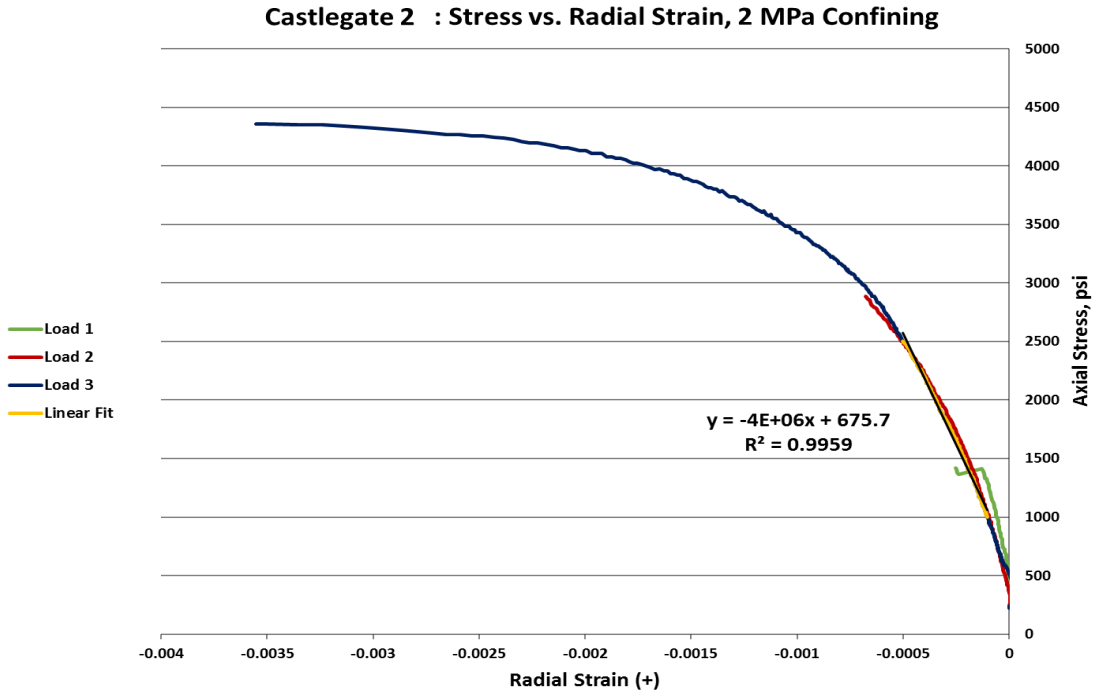
Castlegate 2 : Stress vs. Radial Strain, 2 MPa Confining
Load 1
Load 2
Load 3
Linear Fit
y = -4E+06x + 675.7
R² = 0.9959
-0.004
-0.0035
-0.003
-0.0025
-0.002
-0.0015
-0.001
-0.0005
0
Radial Strain (+)
Axial Stress, psi
5000
4500
4000
3500
3000
2500
2000
1500
1000
500
0

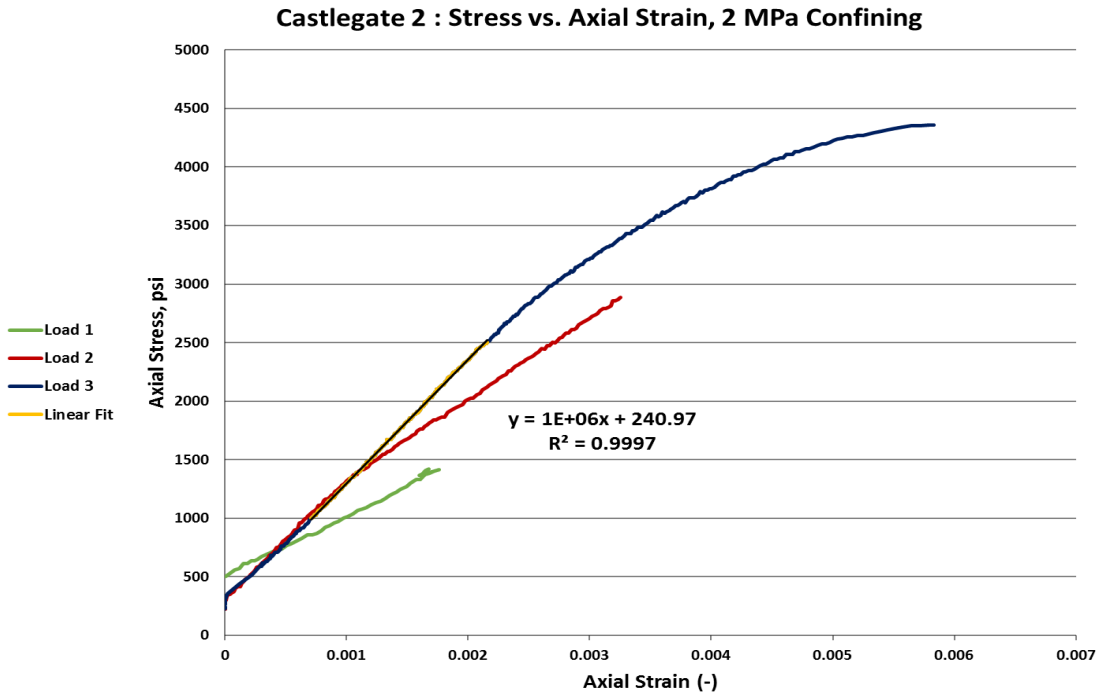
Castlegate 2 : Stress vs. Axial Strain, 2 MPa Confining
Load 1
Load 2
Load 3
Linear Fit
Axial Stress, psi
5000
4500
4000
3500
3000
2500
2000
1500
1000
500
0
y = 1E+06x + 240.97
R² = 0.9997
0
0.001
0.002
0.003
0.004
0.005
0.006
0.007
Axial Strain (-)

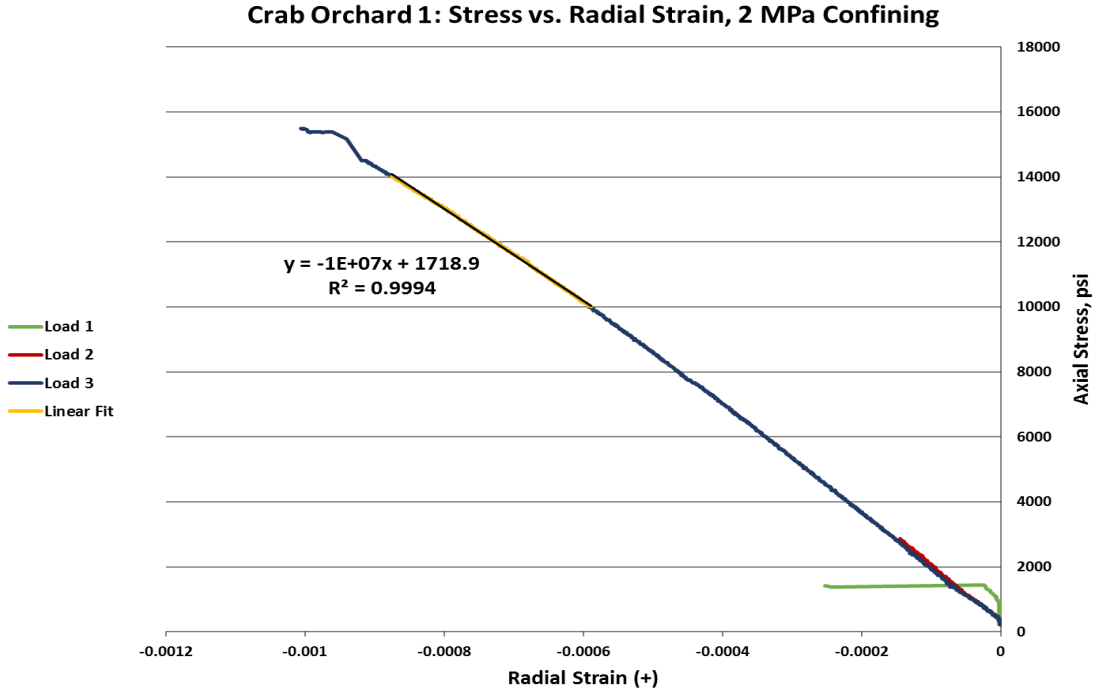
Crab Orchard 1: Stress vs. Radial Strain, 2 MPa Confining
Load 1
Load 2
Load 3
Linear Fit
y = -1E+07x + 1718.9
R² = 0.9994
18000
16000
14000
12000
10000
8000
6000
4000
2000
0
Axial Stress, psi
-0.0012
-0.001
-0.0008
-0.0006
-0.0004
-0.0002
0
Radial Strain (+)

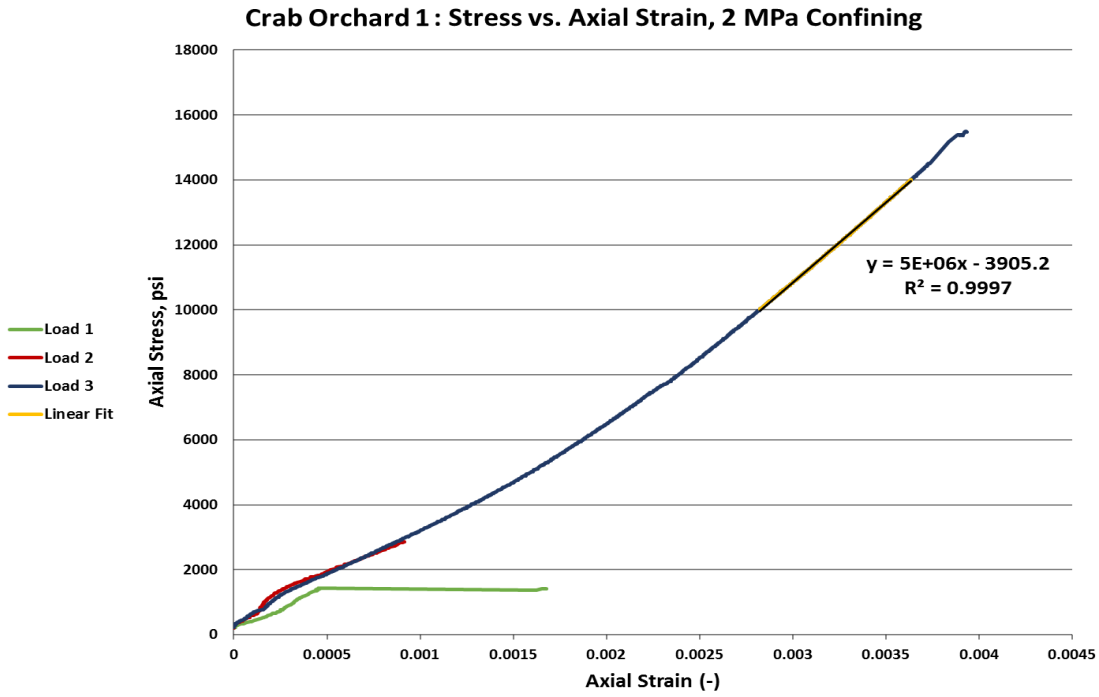
Crab Orchard 1 : Stress vs. Axial Strain, 2 MPa Confining
Load 1
Load 2
Load 3
Linear Fit
Axial Stress, psi
18000
16000
14000
12000
10000
8000
6000
4000
2000
0
y = 5E+06x - 3905.2
R² = 0.9997
0
0.0005
0.001
0.0015
0.002
0.0025
0.003
0.0035
0.004
0.0045
Axial Strain (-)

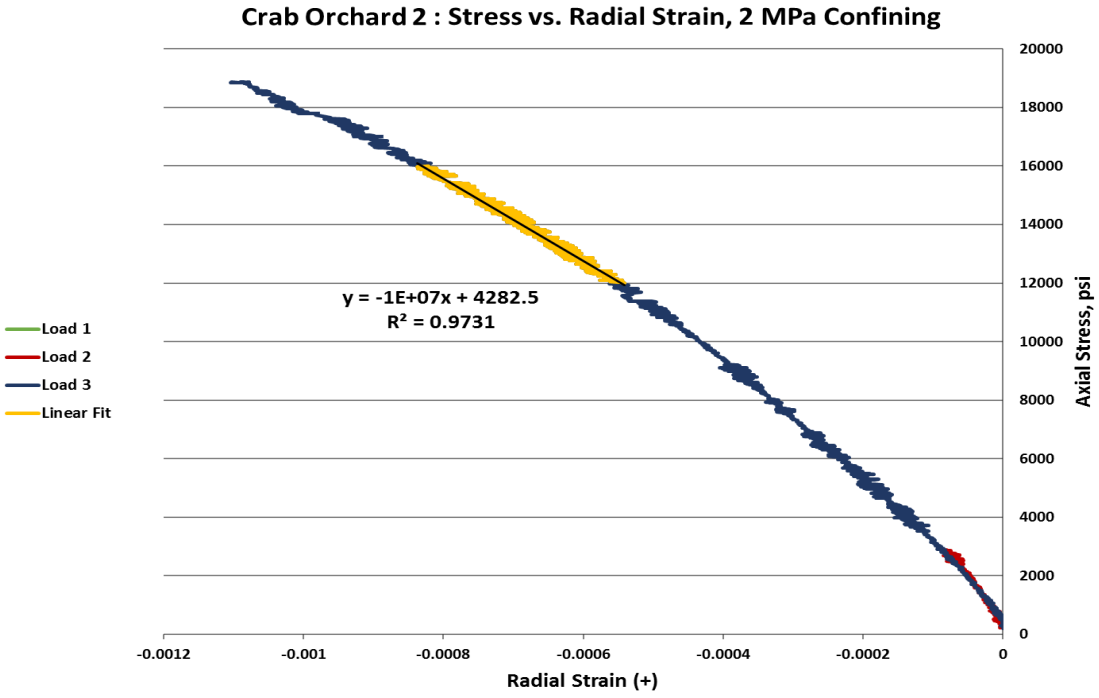
Crab Orchard 2 : Stress vs. Radial Strain, 2 MPa Confining
Load 1
Load 2
Load 3
Linear Fit
y = -1E+07x + 4282.5
R² = 0.9731
20000
18000
16000
14000
12000
10000
8000
6000
4000
2000
0
Axial Stress, psi
-0.0012
-0.001
-0.0008
-0.0006
-0.0004
-0.0002
0
Radial Strain (+)

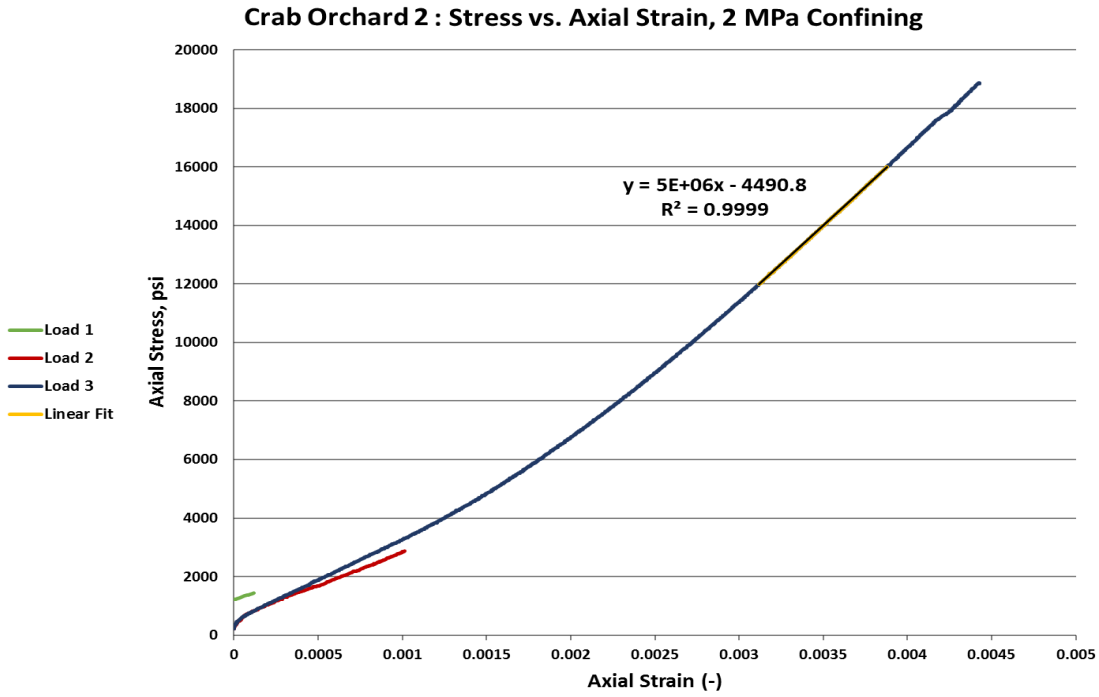
Crab Orchard 2 : Stress vs. Axial Strain, 2 MPa Confining
y = 5E+06x - 4490.8
R² = 0.9999
Load 1
Load 2
Load 3
Linear Fit
Axial Stress, psi
Axial Strain (-)
20000
18000
16000
14000
12000
10000
8000
6000
4000
2000
0
0
0.0005
0.001
0.0015
0.002
0.0025
0.003
0.0035
0.004
0.0045
0.005

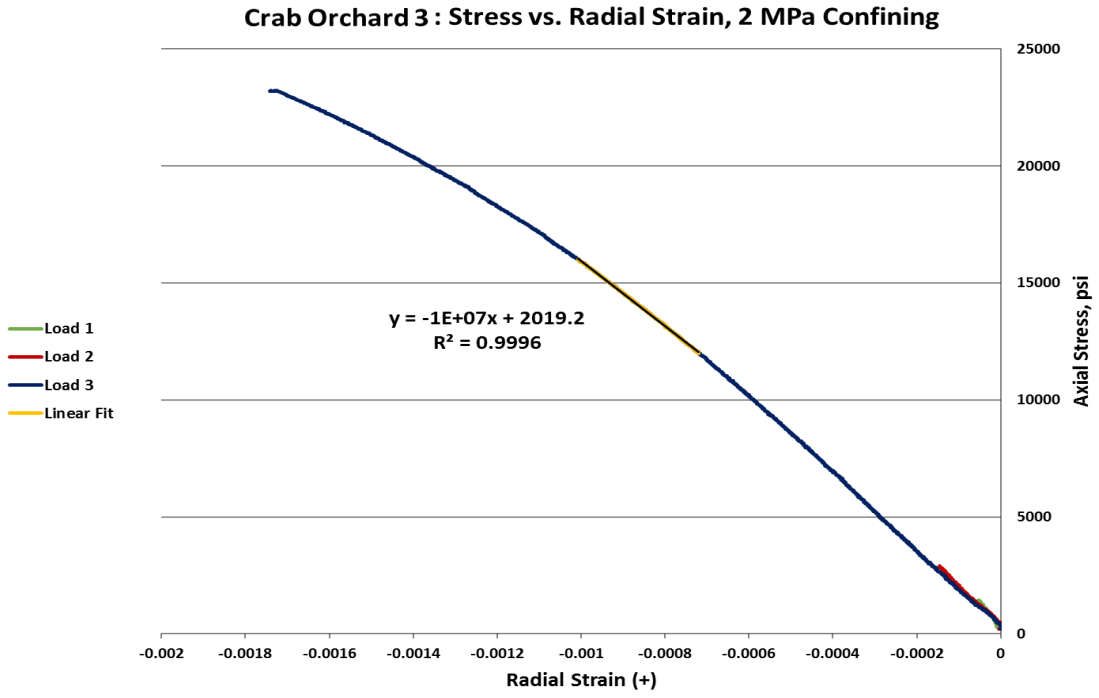
Crab Orchard 3 : Stress vs. Radial Strain, 2 MPa Confining
y = -1E+07x + 2019.2
R² = 0.9996
Load 1
Load 2
Load 3
Linear Fit
Axial Stress, psi
Radial Strain (+)
25000
20000
15000
10000
5000
0
-0.002
-0.0018
-0.0016
-0.0014
-0.0012
-0.001
-0.0008
-0.0006
-0.0004
-0.0002
0

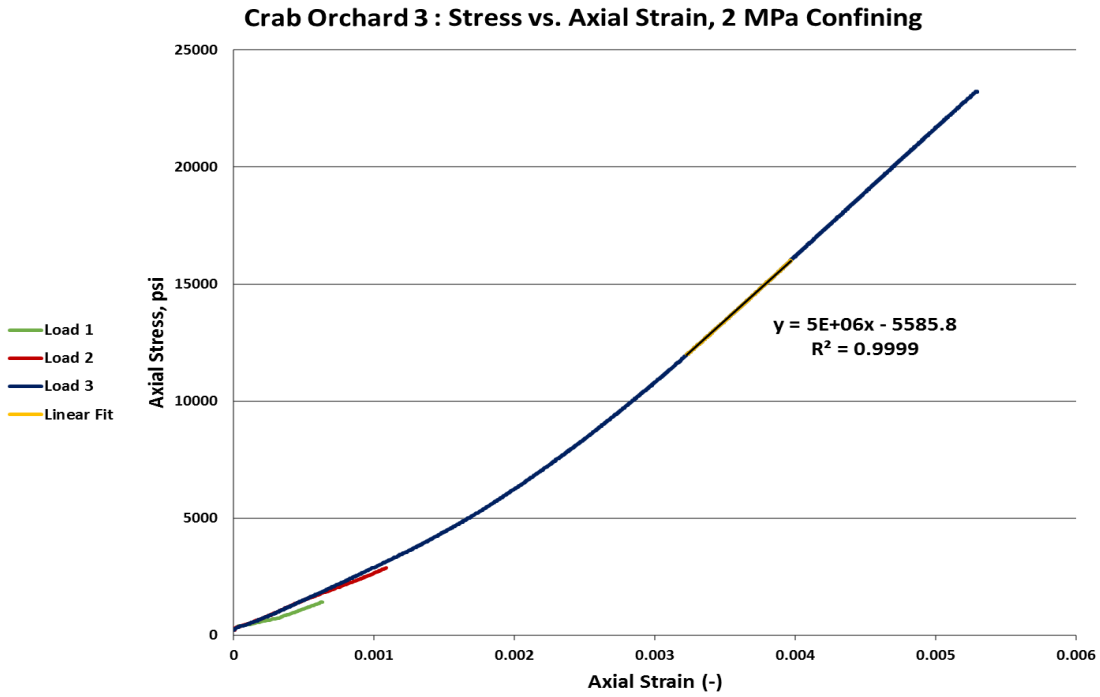
Crab Orchard 3 : Stress vs. Axial Strain, 2 MPa Confining
Load 1
Load 2
Load 3
Linear Fit
Axial Stress, psi
25000
20000
15000
10000
5000
0
y = 5E+06x - 5585.8
R² = 0.9999
0
0.001
0.002
0.003
0.004
0.005
0.006
Axial Strain (-)

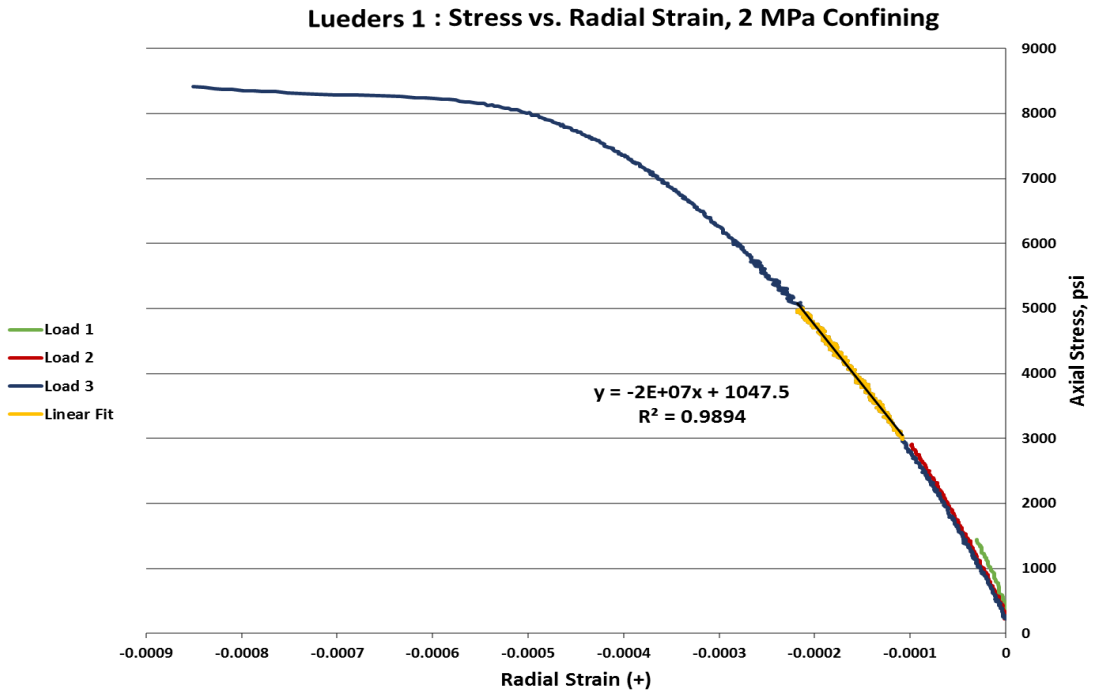
Lueders 1 : Stress vs. Radial Strain, 2 MPa Confining
Load 1
Load 2
Load 3
Linear Fit
y = -2E+07x + 1047.5
R² = 0.9894
9000
8000
7000
6000
5000
4000
3000
2000
1000
0
Axial Stress, psi
-0.0009
-0.0008
-0.0007
-0.0006
-0.0005
-0.0004
-0.0003
-0.0002
-0.0001
0
Radial Strain (+)

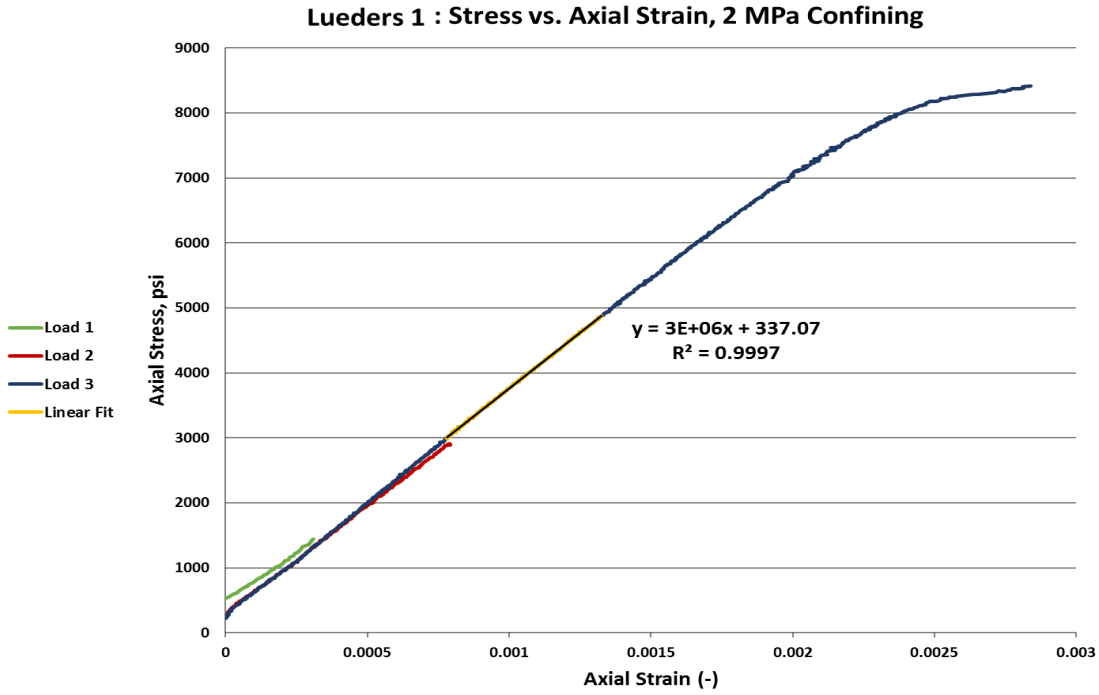
Lueders 1 : Stress vs. Axial Strain, 2 MPa Confining
Load 1
Load 2
Load 3
Linear Fit
Axial Stress, psi
y = 3E+06x + 337.07
R² = 0.9997
Axial Strain (-)
9000
8000
7000
6000
5000
4000
3000
2000
1000
0
0
0.0005
0.001
0.0015
0.002
0.0025
0.003

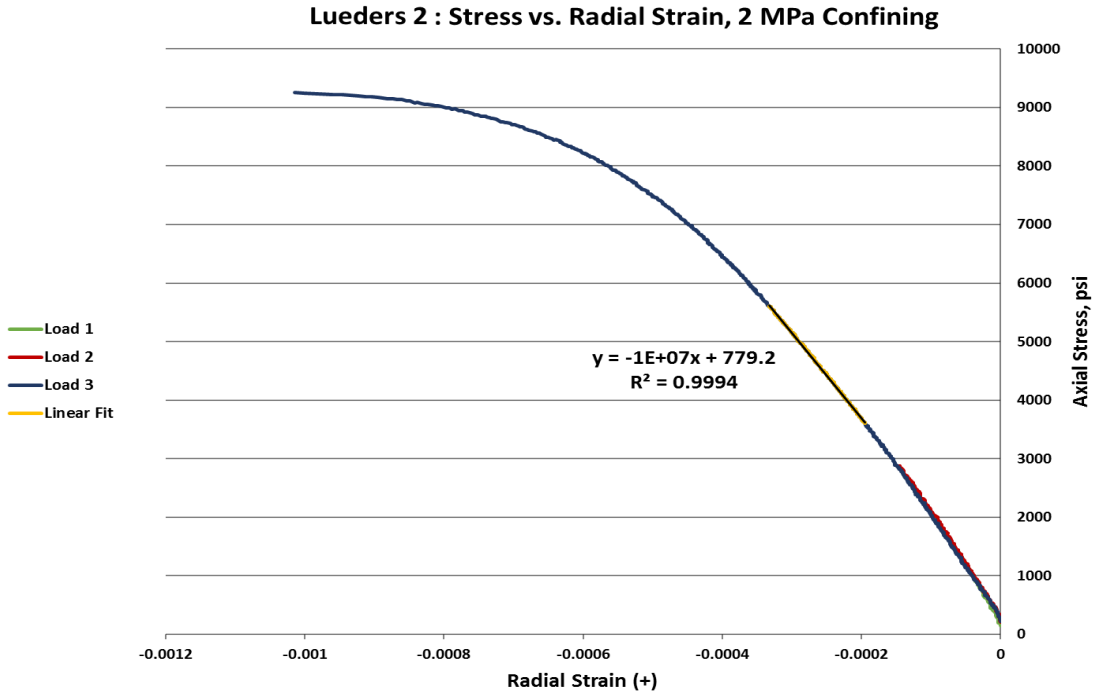
Lueders 2 : Stress vs. Radial Strain, 2 MPa Confining
Load 1
Load 2
Load 3
Linear Fit
y = -1E+07x + 779.2
R² = 0.9994
Axial Stress, psi
Radial Strain (+)
10000
9000
8000
7000
6000
5000
4000
3000
2000
1000
0
-0.0012
-0.001
-0.0008
-0.0006
-0.0004
-0.0002
0

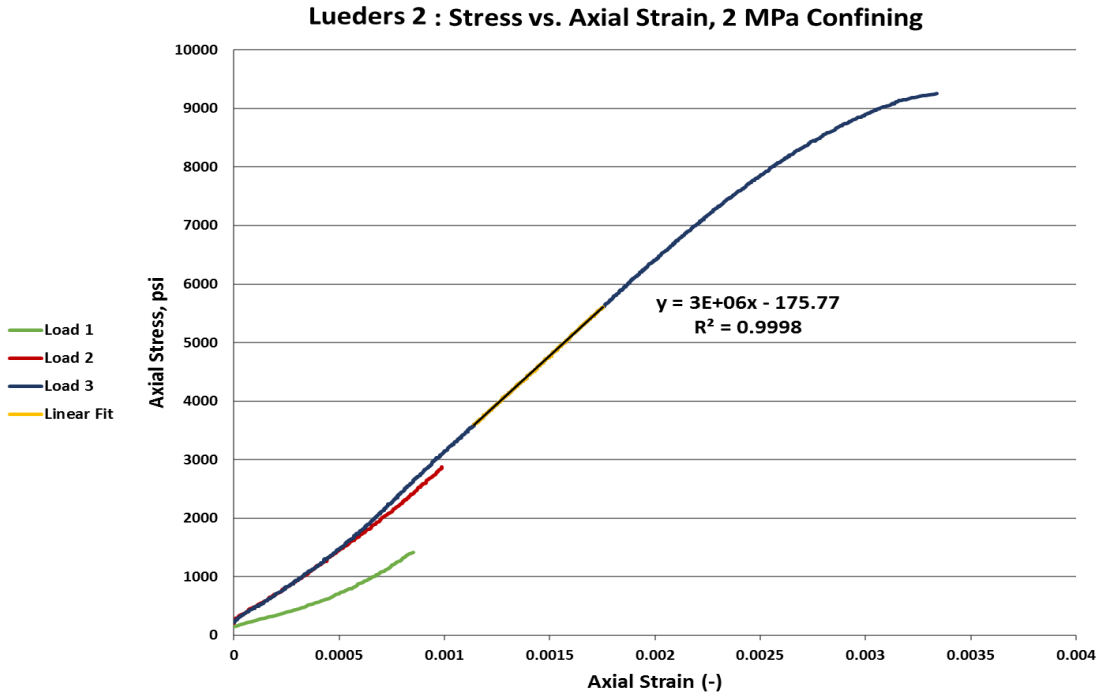
Lueders 2 : Stress vs. Axial Strain, 2 MPa Confining
Load 1
Load 2
Load 3
Linear Fit
Axial Stress, psi
Axial Strain (-)
y = 3E+06x - 175.77
R² = 0.9998
10000
9000
8000
7000
6000
5000
4000
3000
2000
1000
0
0
0.0005
0.001
0.0015
0.002
0.0025
0.003
0.0035
0.004